Article

Cell

Reconstituted Postsynaptic Density as a Molecular Platform for Understanding Synapse Formation and Plasticity

Graphical Abstract

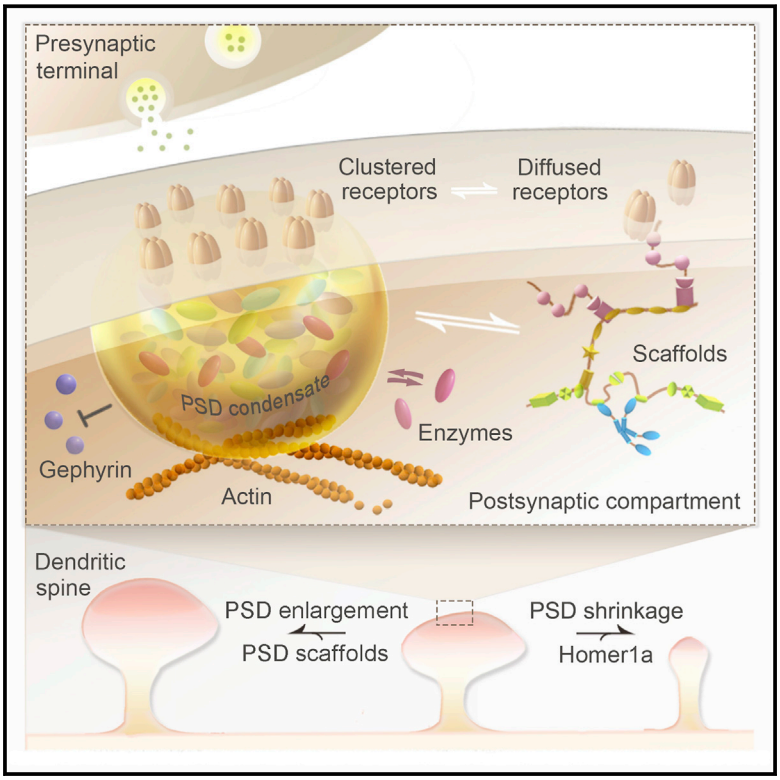

Highlights

- Biochemical reconstitution reveals PSD assembly formation via phase separation
- The ePSD condensates cluster NMDA receptor and promote actin bundle formation
- The ePSD condensates selectively enrich SynGAP and actively exclude gephyrin
- The ePSD condensates can be modulated by activity-dependent protein modifications

Authors

Menglong Zeng, Xudong Chen, Dongshi Guan, Jia Xu, Haowei Wu, Penger Tong, Mingjie Zhang

Correspondence

mzhang@ust.hk

In Brief

Phase transition-mediated formation of excitatory postsynaptic density condensates revealed by biochemical reconstitutions.

Zeng et al., 2018, Cell *174*, 1–16
September 6, 2018
https://doi.org/10.1016/j.cell.2018.06.047

CellPress

Please cite this article in press as: Zeng et al., Reconstituted Postsynaptic Density as a Molecular Platform for Understanding Synapse Formation and Plasticity, Cell (2018), https://doi.org/10.1016/j.cell.2018.06.047

Article

Cell

Reconstituted Postsynaptic Density as a Molecular Platform for Understanding Synapse Formation and Plasticity

Menglong Zeng,[1,5] Xudong Chen,[1,5] Dongshi Guan,[3,4] Jia Xu,[1] Haowei Wu,[1] Penger Tong,[3] and Mingjie Zhang[1,2,6,*]
[1]Division of Life Science, State Key Laboratory of Molecular Neuroscience, Hong Kong University of Science and Technology, Clear Water Bay, Kowloon, Hong Kong, China
[2]Center of Systems Biology and Human Health, Hong Kong University of Science and Technology, Clear Water Bay, Kowloon, Hong Kong, China
[3]Department of Physics, Hong Kong University of Science and Technology, Clear Water Bay, Kowloon, Hong Kong, China
[4]Institute for Advanced Study, Hong Kong University of Science and Technology, Clear Water Bay, Kowloon, Hong Kong, China
[5]These authors contributed equally
[6]Lead Contact
*Correspondence: mzhang@ust.hk
https://doi.org/10.1016/j.cell.2018.06.047

SUMMARY

Synapses are semi-membraneless, protein-dense, sub-micron chemical reaction compartments responsible for signal processing in each and every neuron. Proper formation and dynamic responses to stimulations of synapses, both during development and in adult, are fundamental to functions of mammalian brains, although the molecular basis governing formation and modulation of compartmentalized synaptic assemblies is unclear. Here, we used a biochemical reconstitution approach to show that, both in solution and on supported membrane bilayers, multivalent interaction networks formed by major excitatory postsynaptic density (PSD) scaffold proteins led to formation of PSD-like assemblies via phase separation. The reconstituted PSD-like assemblies can cluster receptors, selectively concentrate enzymes, promote actin bundle formation, and expel inhibitory postsynaptic proteins. Additionally, the condensed phase PSD assemblies have features that are distinct from those in homogeneous solutions and fit for synaptic functions. Thus, we have built a molecular platform for understanding how neuronal synapses are formed and dynamically regulated.

INTRODUCTION

Postsynaptic densities (PSDs) of neuronal synapses were initially recognized by electron microscopy (EM) with observations of electron-dense thickenings beneath postsynaptic membranes (Palay, 1956). Subsequent biochemical and EM analyses of purified PSDs revealed that these structures are composed of densely packed proteins forming disc-shaped mega-assemblies with a few hundred nanometers in width and ~30–50 nm thick (Cohen et al., 1977; Harris and Weinberg, 2012). In response to diverse neuronal stimuli, PSD proteins undergo assembly/disassembly, which are tightly associated with various forms of synaptic plasticity.

A number of unique properties of synapses have hampered detailed understandings of synapse formation and regulation at the molecular level. First, it is hard to find two identical synapses in an entire brain, implying that there is no simple repeating structural unit within synapses. This has prevented detailed structural studies of synapses by existing biophysical methods. Second, synapses are highly compartmentalized, self-assembled reaction machineries with a spine head volume of ~0.1 μm^3 (Harris and Stevens, 1989; Kubota et al., 2007; Nishiyama and Yasuda, 2015). This elaborate and complex compartmentalization is necessary for intricate functions/wiring of neurons, but also creates practical difficulties in understanding each individual synapse. Third, the volume of a spine head is proportional to the size of PSD (Harris and Stevens, 1989; Matsuzaki et al., 2001). Thus, the morphology of synapses is closely coupled with synaptic functions, although with a poorly understood mechanism. Fourth, synapses are extremely plastic. A synapse can undergo chemical component changes on a timescale as fast as a few seconds. Two neighboring spines separated by <1 μm apart can undergo distinct morphology changes upon differential stimulations (Bartol et al., 2015; Matsuzaki et al., 2004; Nishiyama and Yasuda, 2015). There is no unifying theory to explain the molecular mechanisms underpinning the synaptic plasticity. Fifth, highly dense protein-rich assemblies in synaptic compartments (i.e., PSDs) are not enclosed by membrane bilayers and appear to form via certain self-assembling mechanisms (Zeng et al., 2016a). We do not understand how such dense synaptic assemblies can form and stably exist without physical barriers.

Here, we demonstrate that mixing purified postsynaptic scaffold proteins at physiological concentrations can form highly condensed, self-organized PSD-like assemblies via liquid-liquid phase separation (LLPS). Such PSD scaffold condensates can cluster glutamate receptors, enrich synaptic enzymes, and promote actin bundle formation. Importantly, the reconstituted PSD

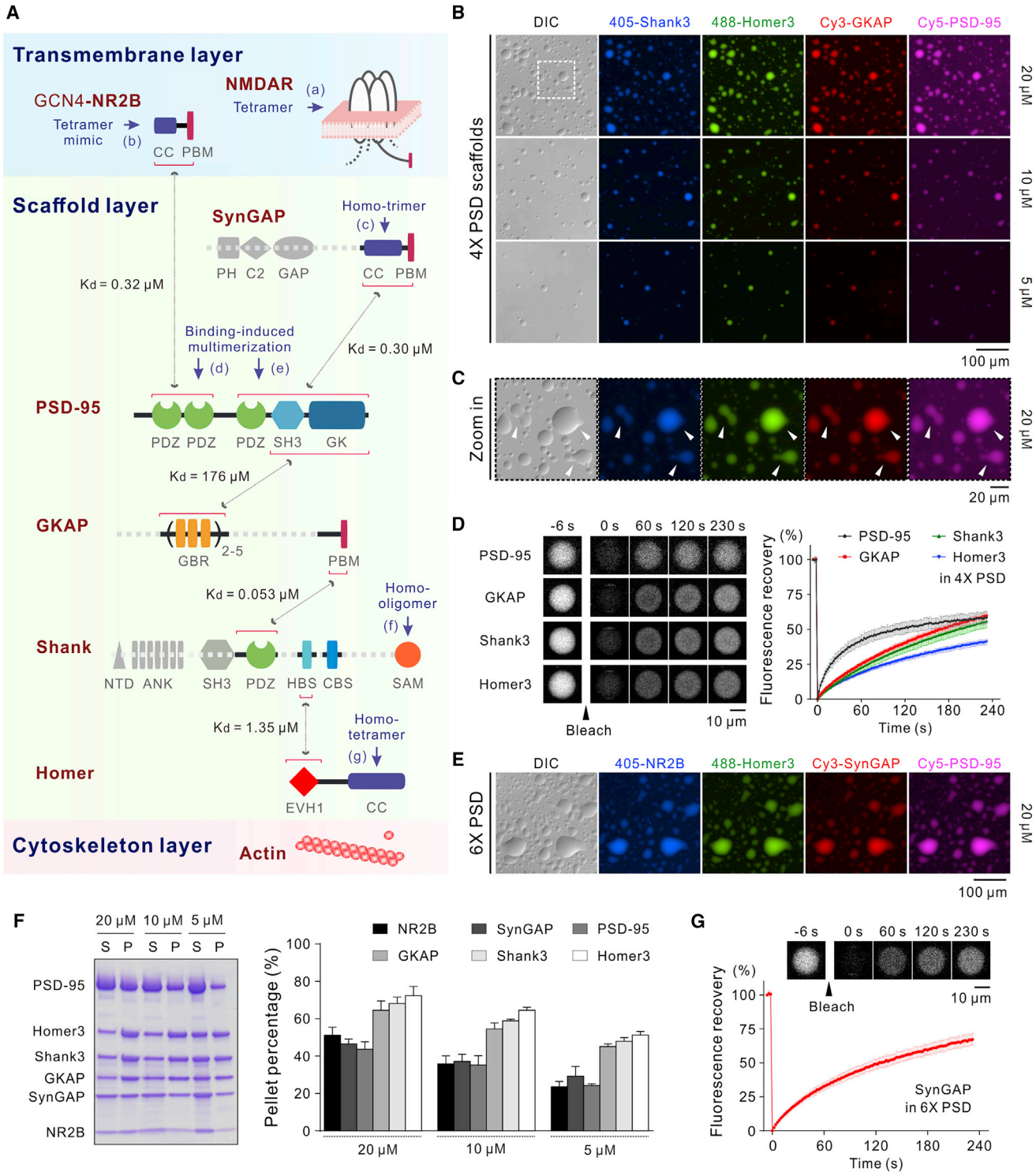

Figure 1. PSD Scaffold Proteins Form Phase Transition-Mediated Condensates Enriching Other Synaptic Proteins

(A) Schematic diagram showing the components and the interaction details of the PSD protein network used in the current study drawn in a spatial order. Solid black lines connecting protein interaction domains/motifs are flexible sequences. Domains drawn in gray and dashed lines are removed from the corresponding proteins for technical reasons. Black arrows indicate the measured binding affinities of the interactions (raw data in Figure S1). Dark blue arrows indicate the multimerization status of the indicated domains or complexes. (a) Lü et al. (2017); (c) Zeng et al. (2016a); (b and d) from Figure S1; (e) Zeng et al. (2018); (f) Baron et al. (2006); (g) Hayashi et al. (2009).

(legend continued on next page)

assemblies actively repel Gephyrin. The LLPS-mediated PSD assembly displays a series of distinct features that are not possessed by canonical protein interaction networks in homogeneous solutions. The reconstituted PSD assemblies may function as molecular platforms for understanding mechanisms governing synaptic formation and plasticity.

RESULTS

PSD Condensates Formation by Mixing Major PSD Scaffold Proteins

We began our reconstitution of PSD assembly using a group of highly abundant scaffold proteins including PSD-95, GKAP, Shank, and Homer. These four proteins, in the order of PSD-95, GKAP (aka SAPAP1 or DLGAP1), Shank, and Homer, serve to connect ion-channels/receptors on the postsynaptic plasma membrane with the actin cytoskeleton in the cytoplasm of PSDs (Figure 1A) (Dosemeci et al., 2016; Petralia et al., 2005; Valtschanoff and Weinberg, 2001; Zhu et al., 2016). We used the full-length PSD-95 and Homer3 for the reconstitution experiments. To obtain soluble and well behaving GKAP and Shank3, we removed part of the sequences of the two proteins (see Figure 1A and STAR Methods for details). The binding affinities between PSD-95 and GKAP, between GKAP and Shank3, and between Shank3 and Homer3 were essentially the same as the bindings investigated using the isolated domains as reported previously (Zeng et al., 2016b; Zhu et al., 2017) (Figures 1A and S1A–S1C). We also confirmed that Homer3 is a homo-tetramer (Hayashi et al., 2006, 2009). Shank3 had a concentration-dependent homo-oligomerization behavior, and both PSD-95 (Figure S1F) and GKAP were highly homogeneous monomers (data not shown).

When mixing fluorescently labeled PSD-95, GKAP, Shank3, and Homer3 at a 1:1:1:1 molar ratio at indicated concentrations (defined as the monomeric unit concentration of each protein throughout the entire study), we readily observed phase separation under light microscopy. Differential interference contrast (DIC) microscopic images revealed that micron-sized, phase-separated droplets had spherical shapes (Figure 1B), and some of the droplets were undergoing fusion process (Figure 1C). Fluorescence images showed each droplet was highly enriched with all four scaffold proteins. Each protein exchanged rapidly between the condensed phase and the surrounding aqueous solution, as revealed by fluorescence recovery after photobleaching (FRAP) analysis (Figure 1D; Video S1). The level of phase transition of the scaffold protein mixtures was correlated to their concentrations. When the concentration of each protein decreased, the amount of the condensed droplets also progressively decreased (Figure 1B). The above results demonstrate that mixing the four major PSD scaffold proteins leads to the formation of self-assembled, highly co-enriched protein networks that appear as liquid condensates.

The PSD Condensates Enrich Glutamate Receptors and Synaptic Enzymes

In addition to interacting with each other, the four scaffold proteins contain a number of domains/motifs capable of binding to the other PSD components. We tested whether the PSD scaffold condensates could incorporate other PSD proteins. We first tested NMDA receptor (NMDAR). To partially mimic the tetrameric nature of NMDAR, we fused the last 5 residues of NR2B to the tail of a tetrameric GCN4 coiled-coil domain (GCN4-NR2B, simply referred as NR2B hereafter) (Harbury et al., 1993). Isothermal titration calorimetry (ITC) assay confirmed that the purified NR2B directly binds to PSD-95 PDZ1-2 (Figures 1A and S1D). We demonstrated that GCN4-NR2B is a homo-tetramer and its binding can induce multimerization of the full-length PSD-95 (Figure S1F). SynGAP is a GTPase activating protein (GAP) highly enriched in PSD (Cheng et al., 2006). We used the C terminus of SynGAPα1 containing a trimeric coiled-coil and a PDZ-binding motif (CC-PBM) domain (referred to as SynGAP hereafter) for this study (Figures 1A and S1E) (Zeng et al., 2016a).

Upon mixing with the four PSD scaffold proteins, both NR2B and SynGAP underwent LLPS and were highly concentrated in the condensed droplets (Figure 1E). The distributions of all six proteins between the aqueous phase (represented by proteins in "supernatant") and the condensed droplets (the "pellet" fraction) were quantified by a sedimentation-based assay. Individually, all six PSD components were highly soluble and did not show any sign of condensed phase formation (Figure S2A). At the concentration of 20 μM (to maximize PSD-95 PDZ1-2 binding, two PSD-95 molar equivalent of NR2B was used here and

(B) DIC and fluorescence images showing that the mixtures of the four PSD scaffold proteins formed phase transition at indicated concentrations. The images were acquired at room temperature with 1% of each protein labeled by the indicated fluorophores. This protein labeling ratio was used throughout the study unless otherwise stated. The dashed box is selected for zoom-in analysis in (C).

(C) Zoom-in analysis of the droplet formation and fusions in the 4× PSD system. The arrow heads highlight those droplets in the process of coalescence into larger ones.

(D) FRAP analysis assaying the exchange kinetics of each protein between the 4× PSD condensates and dilute solution. The concentration of each protein was 20 μM. Related to Video S1.

(E) DIC and fluorescence images showing SynGAP and NR2B were concentrated into droplets in the 6× PSD system. The concentration of each component was 20 μM. GKAP and Shank3 were not labeled and thus not visible.

(F) Representative SDS-PAGE and quantification data showing the distributions of the six PSD components recovered in the dilute phase/supernatant (S) and condensed phase/pellet (P) at indicated protein concentrations. Results were from 3 independent batches of sedimentation assays and represented as mean ± SD.

(G) FRAP analysis showing that SynGAP enriched in the condensed 6× PSD droplets dynamically exchanges with those in the dilute phase. The concentration of each component was at 20 μM.

For all FRAP analyses in this figure, only the protein to be analyzed was Cy3-labeled. The curves represented the averaged signals from 12 droplets with a diameter ~17 μm. All data are presented as mean ± SD.

See also Figures S1, S2, and S3.

throughout the rest of the study), ~50% of PSD-95/SynGAP/NR2B and ~70% of GKAP/Shank3/Homer3 proteins were recovered from the condensed phase (Figure 1F). Consistent with the imaging-based analysis (Figure 1B), the amount of proteins in the condensed droplets gradually decreased with lowered protein concentrations (Figure 1F). After photobleaching, the Cy3-SynGAP intensities in the condensed droplets recovered within minutes (Figure 1G). It indicates that SynGAP enrichment in the condensed droplets is also dynamic, as observed for the enzyme in PSDs of living neurons (Araki et al., 2015). We have also tested phase transition properties of the 6× PSD system with its component stoichiometry matching those derived from proteomic studies and from fluorescence imaging studies (Cheng et al., 2006; Sugiyama et al., 2005) and confirmed that all six components underwent phase separation under these conditions (Figure S2B). In summary, the condensed phase formed by the four PSD scaffold proteins can dramatically enrich NMDA receptors and SynGAP.

Multivalent and Specific Protein-Protein Interactions Drive PSD Condensates Formation via LLPS

Specific and multivalent protein-protein interactions among PSD components are thought to promote PSD formation (Hayashi et al., 2009), although direct experimental evidences supporting this conclusion are difficult to acquire in living neurons. Therefore, we tested such hypothesis using our reconstituted PSD system.

First, we used Cy3-labeled full-length PSD-95 to investigate concentration- and network complexity-dependent phase transition of the PSD assemblies (red panels, Figure 2A). At 40 μM, PSD-95 alone was highly homogeneous and did not form any condensed droplet in solution. Both NR2B and SynGAP are capable of inducing PSD-95 multimer formation (Figure S1F) (Zeng et al., 2018). Upon addition of NR2B and SynGAP, condensed droplets appeared though with small sizes and low in numbers. Next, we added GKAP, Shank3, and Homer3 in a stepwise manner following their order along the axonal-dendritic axis of PSD (from right to left in Figure 2A). Addition of GKAP, which contains three PSD-95 GK domain-binding repeats (GBRs), dramatically increased the condensed droplet formation and lowered the threshold concentration required for LLPS. Addition of Shank3, which contains a self-oligomerizing SAM domain, further promoted phase transition and lowered threshold concentration of LLPS. This trend was further manifested by the addition of the tetrameric Homer3 (Figure 2A). With all of the six components present, formation of the condensed droplets was readily observed at individual protein concentration of 1 μM or lower (Figure 2A), indicating that PSD condensates could form at the physiological concentrations of PSD proteins in dendritic spines.

We next reversed the assembly order of the six PSD proteins using Alexa 488-labeled tetrameric Homer3. Homer3 alone was uniformly distributed in the solution (Figure 2B). The threshold for the Homer3 and Shank3 mixture to undergo LLPS was ~80 μM (Figure S2C). Stepwise additions of GKAP, PSD-95, SynGAP, and NR2B progressively increased the phase transition efficiency and lowered the threshold concentration to undergo LLPS (Figure 2B).

Material Properties of the Reconstituted PSD Condensates

PSD assembly *in vivo* may have semi-solid and gel-like features instead of being a totally fluid-like dilute solution. However, direct measurement of the material properties of PSDs in living neurons is difficult. Additionally, there are limited methods available to study the material properties of biological condensates formed via LLPS, although LLPS is increasingly recognized to be important in diverse cell biology-related processes (Alberti, 2017; Banani et al., 2017; Brangwynne et al., 2009; Feric et al., 2016; Shin and Brangwynne, 2017). Here, we used atomic force microscopy (AFM) to characterize the mechanical properties of PSD droplets. A colloidal probe with a glass bead was adhered under the tip of a triangular AFM cantilever. The AFM probe was gradually lowered with a constant speed toward a condensed droplet in solution (Figure 2C). AFM measured the force generated by the condensed droplet deformation after the probe compressed the droplet. By fitting the slope of the approach curves using the Hertz model, an elastic modulus (E) of the contacted condensed droplet was measured (Figure 2D).

We measured the elastic modulus of droplets formed by 6× PSD and by 2× PSD (SynGAP CC-PBM&PSD-95 PDZ3-SH3-GK) (Zeng et al., 2016a). The droplets formed by 6× PSD showed a sharper approach curve (Figure 2D) and hence a larger measured elastic modulus (E = 3.5 kPa) than the droplets formed by 2× PSD (E = 2.5 kPa) (Figure 2E), indicating that the 6× PSD droplets are more elastic. We also compressed the droplets with different probe indentation speeds. The measured elastic modulus of droplets formed by 6× PSD exhibited a weak power law dependence on the speed (Figures S3A and S3B), which is characteristic of soft glassy materials as a consequence of disorder and metastability of their internal structures (Kollmannsberger and Fabry, 2011). The power law exponent of α = 0.345 indicates that the droplets formed by 6× PSD are more toward solid-like material, as the α value for pure-elastic solid and totally fluid solution is 0 and 1, respectively. The measured elastic modulus was not related to the size of droplets measured (Figure S3C). These results indicate that the expanded multivalent protein-protein network not only reduces the threshold concentration required for LLPS (Figures 2A and 2B), but also changes the material properties of the formed condensates. Because the valency of PSD assemblies in real synapses are higher than our *in vitro* system, the PSDs in neurons are likely to be more toward gel- or glass-like structures as implied by EM observations (Petersen et al., 2003). Finally, we found that the 6× PSD system displays obvious aging and hardening over the time (see Figures S3D–S3G and legends for details).

Quantification of Protein Concentration in the Condensed Phase

Although formation of condensed phase can dramatically concentrate molecules in biological condensates, determining the exact concentrations of components in the condensed droplets has been difficult. Here, we developed a simple confocal microscope imaging-based method for accurately quantifying protein concentrations within the PSD droplets. We illustrate the method using Homer3 concentration quantification in the 4× PSD system as the examples (Figure 3A). Droplets formed

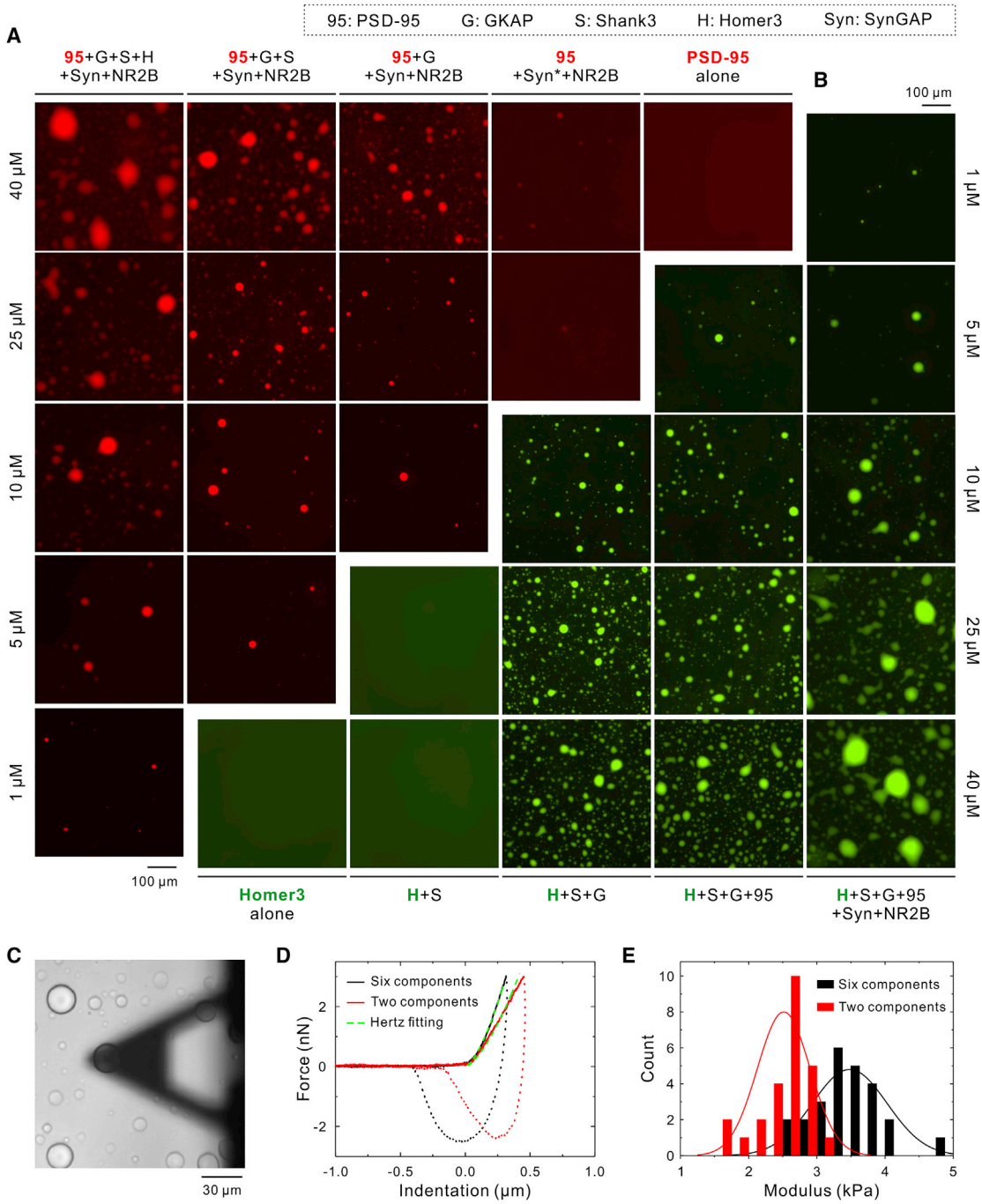

Figure 2. Multivalent Interactions between Scaffold Proteins Drive PSD Condensates Formation

(A and B) Valency- and protein concentration-dependent PSD condensates formation. In (A), only PSD-95 was Cy3-labeled. In (B), only Homer3 was Alexa 488-labeled. In the "95+Syn*+NR2B" group in (A), SynGAP:PSD-95 ratio was set at a molar ratio of 3:1 as one SynGAP trimer to one full-length PSD-95. In all other groups, components were mixed at equimolar concentration with the exception that NR2B was at doubled molar ratio of the rest of the components. For each group of the mixtures at a given protein concentration, the fluorescence imaging settings were identical for easy comparison. Images were acquired at ~5 min after injecting the mixture into the chamber.

(C) Top-on view image of the condensed droplets under the indentation of an AFM probe.

(D) The force-indentation curves measured on the PSD droplets with the approach curves in sloid lines and the retraction curves in dotted line. The green dashed lines show the fitting of the Hertz model to the approach curves.

(E) The distribution of the measured elastic modulus *E* of the PSD droplets. The total number of the measured droplets (n) is 25 for each type of PSD droplets. The solid lines show the fit to the normal distribution with the peak value *E* = 3.5 kPa for the 6× PSD droplets and *E* = 2.5 kPa for 2× PSD droplets.

See also Figures S2 and S3.

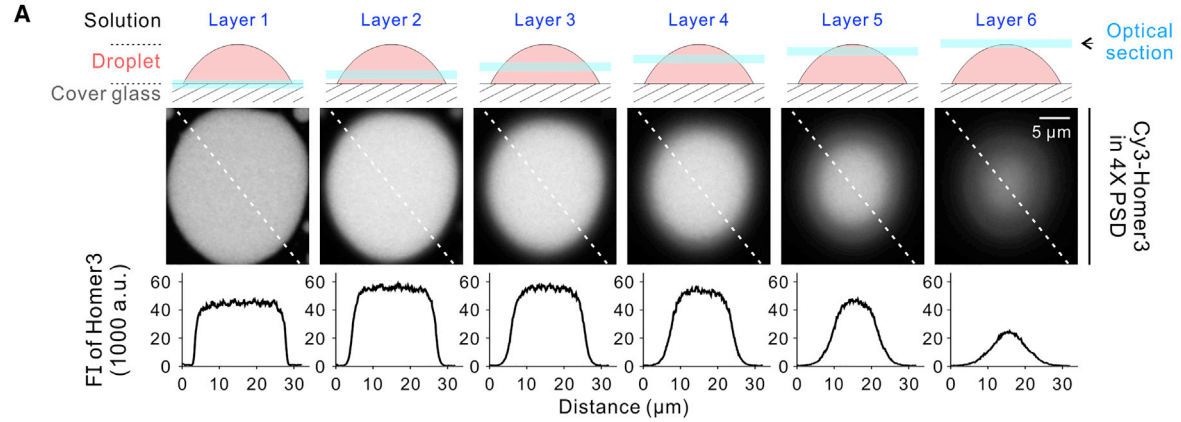

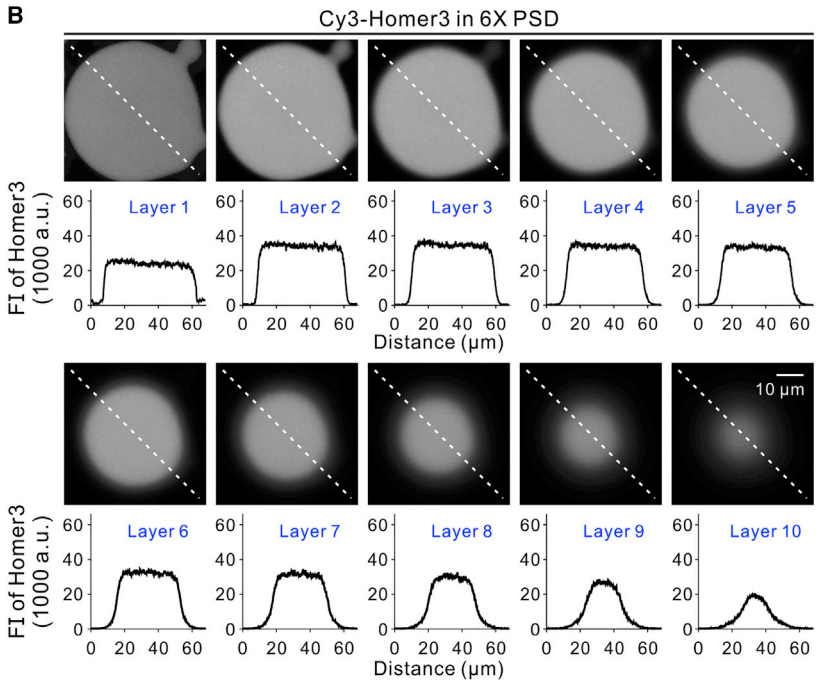

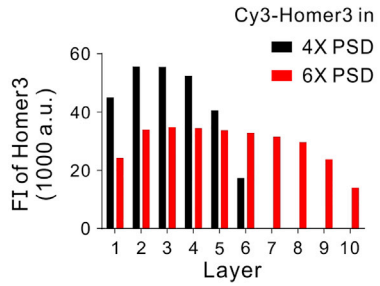

D

	4X PSD	6X PSD
Layer with I_{max}	2	3
Layers with I (I > 0.9 I_{max})	2, 3, 4	2, 3, 4 5, 6, 7
Mean intensity of layers with I (1000 a.u.)	54.4	33.5

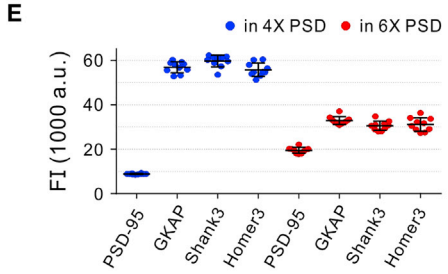

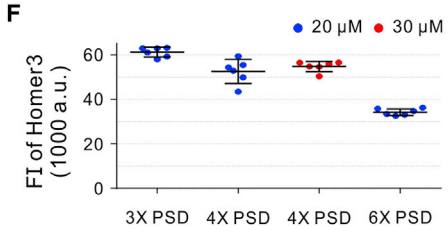

G

Cy3-protein	Composition & conc. (μM)	Droplet Cy3 intensity (1000 a.u.)	Droplet Cy3-protein conc. (μM)	Droplet total protein conc. (μM)
PSD-95	4X PSD & 20	8.9± 0.2	4.1 ± 0.5	410 ± 50
GKAP		56.9 ± 2.5	24.3 ± 1.4	2430 ± 140
Shank3		59.7 ± 2.6	25.5 ± 1.5	2550 ± 150
Homer3		55.8 ± 3.0	23.9 ± 1.6	2390 ± 160
PSD-95	6X PSD & 20	19.5 ± 1.3	8.6 ± 0.9	860 ± 90
GKAP		32.9 ± 1.8	14.2 ± 1.1	1420 ± 110
Shank3		30.6 ± 2.1	13.2 ± 1.3	1320 ± 130
Homer3		30.9 ± 3.0	13.4 ± 1.6	1340 ± 160
Homer3	3X PSD & 20	61.3 ± 2.2	26.2 ± 1.3	2620 ± 130
	4X PSD & 20	52.6 ± 5.5	22.5 ± 2.7	2250 ± 270
	4X PSD & 30	54.8 ± 2.3	23.4 ± 1.3	2340 ± 130
	6X PSD & 20	34.2 ± 1.4	14.8 ± 1.0	1480 ± 100

(legend on next page)

in flow chambers were imaged by a confocal microscope in a z stack mode with a step interval of 1.0 μm and an optical section thickness of ~0.9 μm. The peak fluorescence intensities of optical layers that are completely within the z-dimension of a droplet (e.g., layers 2–4 in Figure 3A and layers 2–7 in Figure 3B) were averaged for determining the concentration of Homer3 in the 4× PSD and 6× PSD condensates (Figures 3B–3D). A standard calibration curve using a Cy3-labeled protein was constructed to convert the Cy3 fluorescence intensity into absolute protein concentration (Figure S4A; see STAR Methods for details).

Using this method, we quantified concentrations of each component (PSD-95/GKAP/Shank3/Homer3) in the 4× 20 μM PSD droplets. In each measurement, only one component was Cy3-labeled to avoid possible signal cross-talk (Figure 3E). The concentrations for GKAP, Shank3, and Homer3 in the condensed phase are similar and at ~2.5 mM, whereas PSD-95 has a ~6-fold lower concentration (Figures 3E and 3G). We also quantified the intensities for these four scaffold proteins in the 6× 20 μM PSD droplets. The concentrations for GKAP, Shank3, and Homer3 in the 6× PSD condensed phase are still similar (~1.3 mM) but reduced to around half of that as those in the 4× PSD droplets (Figures 3E and 3G). The PSD-95 concentration in the 6× PSD droplets is approximately double of that in the 4× PSD droplets (Figures 3E and 3G).

We next compared Homer3 concentrations in various droplets composed of (1) 3× 20 μM PSD (H + S + G), (2) 4× 20 μM PSD (H + S + G + 95), (3) 4× 30 μM PSD (H + S + G + 95), and (4) 6× 20 μM PSD (H + S + G + 95 + Syn + NR2B) (Figures 3F and 3G). This quantification data showed: (1) Homer3 concentration in 3× PSD droplets is slightly higher than that in 4× PSD droplets and is about twice as that in 6× PSD, and (2) higher initial concentration of each component (30 μM versus 20 μM) does not change the final concentration in the droplets in 4× PSD. This means that once a system reaches the phase separation threshold, the component concentration in the condensed phase does not increase but the volume will grow when the initial material concentration further increases, (3) combining the data in Figure 2, the phase separation threshold concentration became lower and lower when the components in the PSD system gets more complicated. It is noted that the final concentration of each component in a more complicated system does not increase continuously. It appears that the total material concentration in a condensed phase will have a limit, and this limit may be determined by the solubility of the assembled condensates, (4) the concentrations of each protein component in droplets with different sizes in a given system are same (Figure S4B).

"Drivers" versus "Clients" in Forming PSD Condensates

We adopted the sedimentation assay to further evaluate the contribution of each protein to the condensate formation in the 6× PSD system. To do this, we dropped out one component at a time and measured the dilution phase versus condensed phase distributions (or S/P ratios) of the rest five components (Figures 4A and 4B). The normalized decreases of PSD components resulted from dropout of one protein in each experiment were plotted in Figure 4C. Deletion of any component in the 6× PSD system resulted in decreases of one or more other proteins, with direct binder(s) as the largest affected component. For instance, the removal of PSD-95 resulted in obvious decreases of its direct binders (NR2B, SynGAP, and GKAP) from being incorporated into the condensed phase; whereas little changes were detected for Shank3 and Homer3 (Figures 4A–4C). When Shank3 was deleted, the alterations on the GKAP and Homer3 were very obvious (larger than 50%), but the changes to NR2B, SynGAP, and PSD-95 were smaller.

Overall, removal of a "riding" protein such as SynGAP had smaller impact on the rest five PSD proteins from entering the condensed phase. In contrast, removing a scaffold protein tends to have larger and overall changes on the PSD condensate formation. The most dramatic example is the removal of GKAP, which led to the overall reduction of all other five components in the condensed phase (Figure 4C). This may be related to the organization feature of the PSD assembly in that GKAP is in the middle layer serving to connect the NR2B/SynGAP/PSD-95 sub-group and the Shank3/Homer3 sub-group in forming the large PSD network (Figure 1A). We further tested the role of GKAP in synergizing the phase transition of the rest 5 PSD proteins by keeping the 5 PSD components at 4 μM and gradually increased GKAP concentration from 0 μM to 8 μM. Increasing GKAP concentration increased the PSD condensates formation in parallel (Figure 4D). Correlated with what was observed, *Sapap3* (the major member of the GKAP/SAPAP family expressed in mouse striatum) knockout mice showed prominently reduced PSD thickness in synapses from striatal neurons (Welch

Figure 3. Confocal Imaging-Based Method to Quantify Concentrations of PSD Components in the Condensed Droplets

(A) Fluorescence intensity analysis of Cy3-Homer3 in each layer of a 4× PSD droplet (20 μM, as in Figure 1C). The top of the panel shows a schematic diagram of moving the confocal plane from near the cover glass to the surface of the droplet (i.e., layer 1 to layer 6). Cy3 fluorescence intensity along the dashed line in each layer is plotted below each image layer.

(B) Fluorescence intensity analysis of Cy3-Homer3 in each layer of a 6× PSD droplet (20 μM, as in Figure 1E).

(C) Plot of measured peak intensity as a function of the layer number for the images from (A) and (B).

(D) Illustration of the droplet intensity quantification. In the 4× PSD system, layers 2–4 are used to calculate the mean peak intensity of Homer3. In the 6× PSD system, layers 2–7 are used to calculate the mean peak intensity of Homer3.

(E) Cy3 fluorescence intensity of each PSD scaffold protein in 4× or 6× PSD droplets. Data for each protein were collected from 10 droplets in each group and presented as mean ± SD. Both the composition and concentrations of 4× PSD droplets (in blue) and 6× PSD droplets (in red) are the same as in Figures 1C and 1E, respectively.

(F) Cy3-Homer3 fluorescence intensity analysis from four different groups (with different composition and concentration between each groups). Data for each protein were collected from 6 droplets in each group and presented as mean ± SD.

(G) Summary of the fluorescence intensities in each group in (E) and (F) and the corresponding protein concentrations calculated by converting fluorescence intensities to molar concentrations using the calibration curve in Figure S4A. Values are represented as mean ± SD.

See also Figure S4.

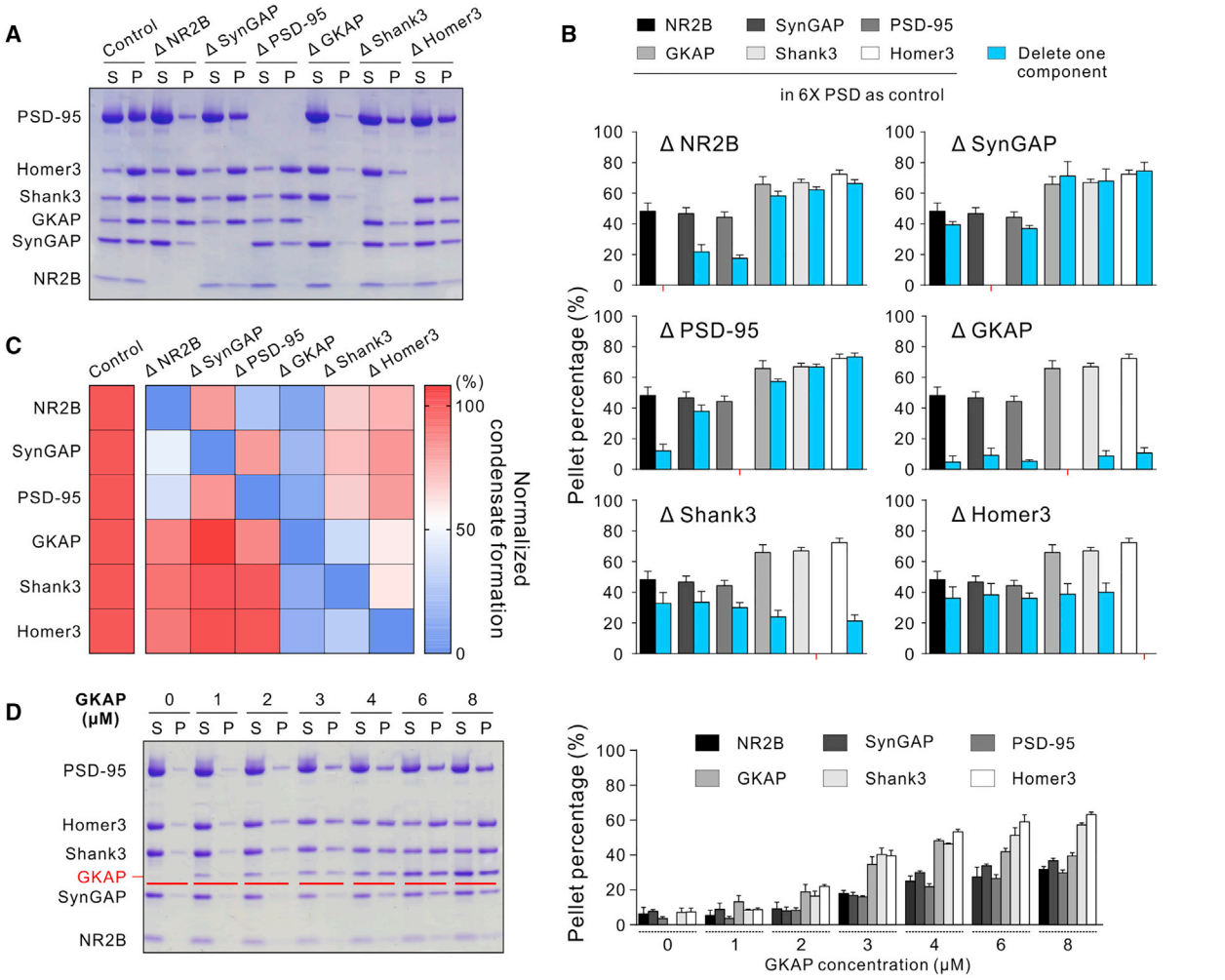

(legend on next page)

et al., 2007). Based on the above observations, we propose that the four scaffold proteins are key "drivers" for the condensed PSD assemblies, whereas SynGAP is a "client" protein recruited by the scaffold proteins.

We also investigated the roles of direct interactions between paired components or valency of selected proteins in PSD condensate formation. Homer1c shares a similar domain organization with Homer3 and also exists as a tetramer (Hayashi et al., 2009). Accordingly, the phase transition efficiency of the 6× PSD system with Homer1c replacing Homer3 is highly similar to that containing Homer3 (Figure 4E). Homer1a is a short splice variant of Homer1 that contains the N-terminal EVH1 domain followed by a ~60-residue Homer1a-specific sequence with no defined structure but lacks the tetrameric CC domain (Hayashi et al., 2006; Sala et al., 2003) (Figure S5F). Replacing Homer3 by Homer1a dramatically decreased the phase transition efficiency of all components in the 6× PSD system (Figure 4E). It is noted that replacing Homer3 with Homer1a caused more dramatic decrease of condensed phase formation than just removing Homer3 (Figures 4A and 4E), indicating a dominant-negative effect of Homer1a on the phase transition of the 6× PSD system. We found that the 60-residue Homer1a-specific sequence following its EVH1 domain plays an important role in preventing the PSD-95/SynGAP/NR2B subgroup from entering the condensed phase (see Figure S5 for more details). Homer3 LR&LE is a Homer3 mutant in which the Leu338 and Leu343 in its CC region were replaced by Arg and Glu, respectively. Homer3 LR&LE binds to Shank3 as the WT protein does, but the mutant became a dimer (data not shown, also see Hayashi et al., 2009). Replacing WT Homer3 with the LR&LE mutant also reduced phase transition efficiency of the 6× PSD system (Figure 4E), underscoring the critical role of Homer tetramerization in promoting LLPS.

Another set of manipulations was made on the "client" protein SynGAP. Deleting the last 4-residue PBM of SynGAP (d4) abolished its interaction with PSD-95 *in vitro* and resulted in reduced synaptic enrichment in neurons (Zeng et al., 2016a). Mirroring this observation, SynGAP d4 exhibited dramatically reduced enrichment in the condensed phase in the 6× PSD system (Figure 4F). An LD&KD mutant of SynGAP, which converted the protein from trimer to monomer but had minimal impact on the PSD-95 binding, has a weaker synaptic localization in living neurons (Zeng et al., 2016a). This LD&KD mutant of SynGAP also had reduced enrichment in the condensed phase (Figure 4F).

Reconstituted PSD Assemblies Undergo Phase Separation on Lipid Membrane Bilayers

In living neurons, one side of the condensed PSDs is attached to the postsynaptic plasma membranes and the other side is exposed to the cytoplasm of dendritic spines, creating a directional PSD network assembly vital for synaptic signal transmissions. To mimic the semi-open PSD assembly, we reconstituted the 6× PSD system on a 2D membrane system using supported lipid bilayers with a defined lipid composition (Figure 5A) (Banjade and Rosen, 2014).

His-NR2B alone captured by the Ni^{2+}-NTA-DGS-containing lipid bilayers was uniformly distributed (Figures 5B and 5C, at 0 min) and freely diffusing on the bilayers as revealed by FRAP analysis (Figure S4C). Upon the addition of other five PSD components (premixed at a concentration of 2 μM each), submicron-sized clusters appeared within a few minutes. Small clusters gradually grew on the entire membrane surface and fused into larger ones with irregular shapes, and finally the majority of clusters coalesced into a mesh-like network (Figure 5C). Meanwhile, the fluorescence intensity in the dilute phase progressively reduced (Figures 5B–5D; Video S2). The phase separation of the 6× PSD system on the lipid bilayers follows the spinodal decomposition mode as observed recently (Banjade and Rosen, 2014; Su et al., 2016). The irregular shaped laminar structures of the condensed PSD assemblies on the lipid bilayers are actually reminiscent of the shapes of PSDs observed in neurons. If the premixed five PSD components contained 2 mM EDTA in the buffer, no mesh-like NR2B could be observed. Instead, tiny spherical shaped condensed droplets were observed in solution (Figure 5E), indicating that tethering PSD scaffold proteins to lipid membranes via His-NR2B is essential for the spinodal decomposition to occur.

Confocal imaging revealed that PSD-95, Shank3, and Homer3 all colocalized within the NR2B-containing clusters (Figure 5F). FRAP analysis showed that proteins in the condensed clusters exhibited dynamic exchanges with those in the aqueous solution (Figure 5G). Mirrored the behavior of the condensates formed in 3D solutions, cluster formation on lipid bilayers also depended on the specific and multivalent interactions between PSD

Figure 4. Contributions of Each Component to the Phase Transition Efficiency

(A) Representative SDS-PAGE and quantification data showing the distributions of the rest of five PSD components recovered in the dilute phase (S) and condensed phase (P) after removing one component at a time in the sedimentation-based assays.

(B) Quantifications of the dropout experiments shown in (A).

(C) Heatmap plot showing the normalized changes of each protein recovered in the condensed phase in the component dropout experiments quantified in the (B). The percentage in 6× PSD group was normalized as 100%. The depleted protein was set as 0%.

(D) Addition of GKAP into other five PSD protein mixture triggers phase separation and formation of PSD condensates. SDS-PAGE and quantitative analysis show the S/P distribution of each component upon addition of increasing amount of GKAP when the rest of the proteins are kept at 4 μM.

(E) Sedimentation-based assay showing the S/P distributions of six PSD components when the tetrameric Homer3 was replaced by the tetrameric Homer1c, the dimeric Homer3 LR&LE mutant, and monomeric Homer1a, respectively.

(F) Sedimentation-based assay showing the S/P distributions of six PSD components when the wild-type SynGAP was replaced by binding deficient SynGAP d4 or monomeric SynGAP LD&KD mutant.

In all sedimentation assays, protein concentrations were set at 20 μM except in (D). Statistic data were presented as mean ± SD with results from 3 independent batches of sedimentation experiments. ns, not significant; *$p < 0.05$; **$p < 0.01$; ***$p < 0.001$; ****$p < 0.0001$ using one-way ANOVA with Dunnett's multiple comparisons test.

See also Figure S5.

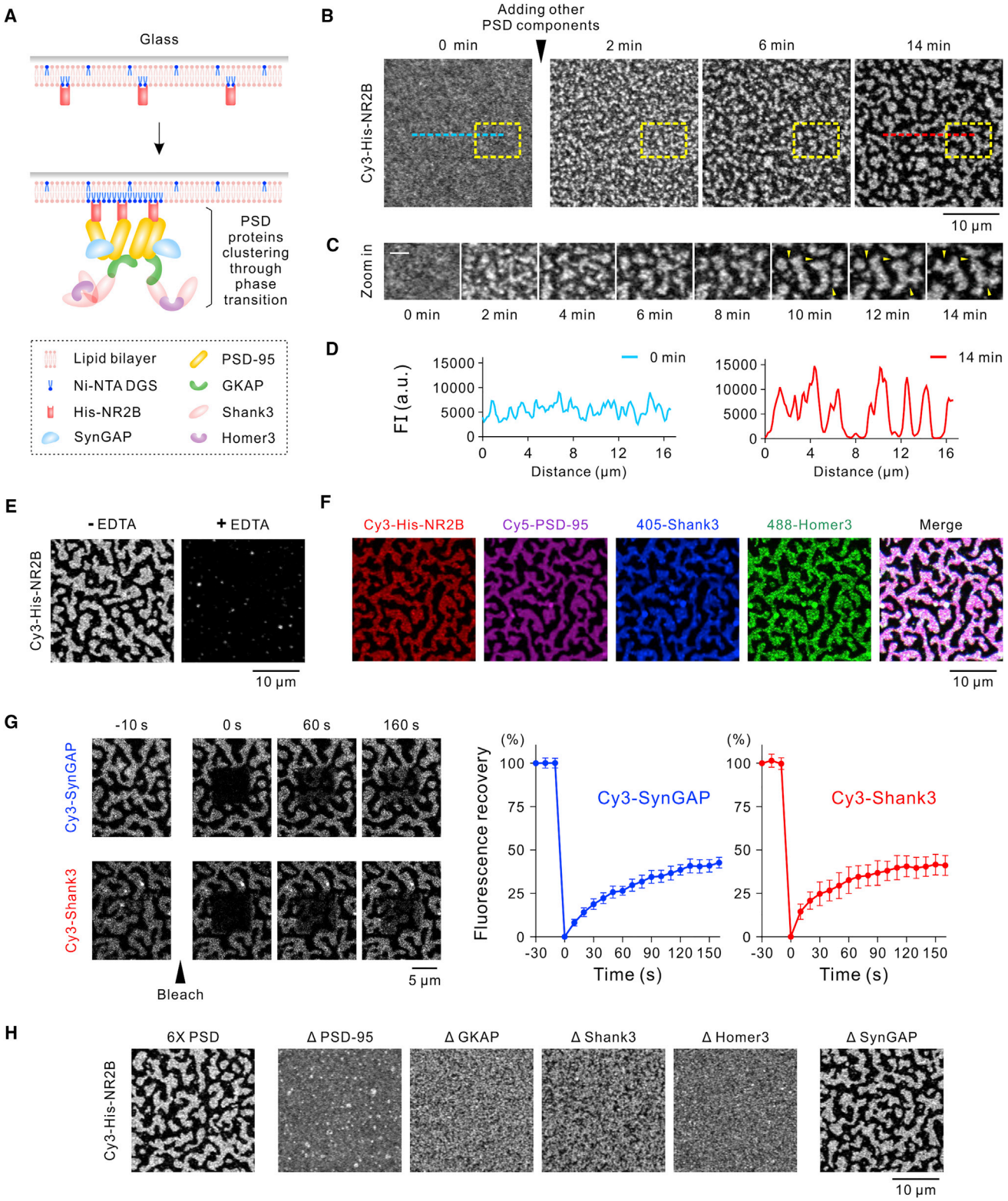

Figure 5. PSD Condensates Formation and NR2B Clustering on Lipid Membrane Bilayers

(A) Schematic diagram showing the principle of PSD phase transition and NR2B clustering on supported lipid membrane bilayers.

(B) Time-lapse confocal images showing that homogeneously distributed Cy3-His-NR2B on membrane bilayers gradually clustered upon addition of the rest of five unlabeled PSD proteins. Related to Video S2. Dashed box and lines are analyzed in (C) and (D) below.

(legend continued on next page)

proteins. Under the assay condition shown in Figure 5B, removal of any one of the four scaffold proteins completely prevented the formation of PSD clusters. In contrast, removal of SynGAP had little impact on the cluster formation of the NR2B (Figure 5H). The above results reveal that the formation of PSD condensates on the lipid bilayers also occur via LLPS. Additionally, formation of the PSD condensates by the major scaffold proteins can massively cluster NR2B receptor on the membrane bilayers and enrich enzymes such as SynGAP.

Network-Level Scaling of the PSD Assembly in the Condensed Phase

We next explored whether the LLPS-mediated PSD assemblies could be modulated by regulatory mechanisms mimicking neuronal activity events, and whether the PSD condensates might contain properties that are distinct to the protein interaction networks commonly studied in dilute aqueous solutions. We picked Homer proteins to study these questions. Overexpression of Homer1a exhibited broad inhibitory effects on dendritic spine morphogenesis, synaptic targeting of PSD scaffold proteins, surface expression of AMPARs, and synaptic transmissions (Sala et al., 2003). Recently, it was shown that sleeping induced massive elevation of Homer1a in excitatory synapses (Diering et al., 2017). Interestingly, EM studies observed global down-scaling of PSD sizes of motor and sensory cortical synapses in mice during sleep (de Vivo et al., 2017).

We tested whether Homer1a might be able to regulate PSD condensate formation. ITC assay showed that Homer1a and Homer1c displayed the same Shank3 binding affinity as Homer3 does (Figures 6A and S1C). In the solution system, we observed progressive droplets dispersions accompanied by gradually increased Cy3-PSD-95 signal in the dilute aqueous phase upon injection of Homer1a into a chamber containing pre-formed 6× PSD droplets (Figure 6B; Video S3). In the sedimentation-based assays, addition of increasing amounts of Homer1a into a fixed amount of Homer1c-containing 6× PSD system (20 μM) progressively prevented all six components from entering the condensed phase (Figure 6C). On the 2D lipid bilayers, addition of Homer1a also disassembled the condensed 6× PSD clusters (Figure 6D; Video S4). An interesting feature is that, although Homer proteins only specifically interact with Shank3 in the 6× PSD system, the formation of the condensed PSD assembly via LLPS allows the entire PSD network to be regulated by alterations of a single protein Homer1a (see Figure S5 for more details). Our observation nicely correlates with the global down-scaling of the PSD sizes in mice induced by sleep (de Vivo et al., 2017). It also indicates that the formation of PSD condensates may allow the PSD network to have distinct properties that are not achievable by the dilute homogeneous solutions.

Reconstituted PSD Condensates Promote Actin Polymerization

Shank is localized in the deep layer of PSD facing dendritic cytoplasm (Petersen et al., 2003; Petralia et al., 2005). It is also known to directly interact with actin cytoskeleton regulatory proteins like cortactin (Naisbitt et al., 1999) and Arp2/3 complex subunits (Han et al., 2013). In Shank3 overexpression transgenic mice, F-actin levels of excitatory synapses increased significantly compared to the wild-type littermates (Han et al., 2013). We next explored whether the reconstituted PSD condensates could also recruit actin-related proteins.

Cortactin has an N-terminal acidic domain that binds to and stimulates Arp2/3 complex, followed by tandem cortactin repeats (CR) that associate with F-actin and a C-terminal SH3 domain binding to the Shank3 (Figures 7A and 7B) (Naisbitt et al., 1999; Weed et al., 2000). Purified cortactin interacted with Shank3 with a K_d ~4.4 μM (Figure 7A). As shown by both sedimentation-based assay and fluorescence imaging assay, cortactin could also be enriched to the condensed phase formed by the 6× PSD system (Figures 7B and 7C). We then added cortactin, Arp2/3 complex together with G-actin into the 6× PSD system assembled on the lipid bilayers. Both G-actin and His-NR2B were initially homogeneously distributed. After adding the other five PSD components, His-NR2B clusters appeared within a few minutes. At ~15 min after phase transition started, polymerized F-actin structures started to emerge in the condensed PSD assemblies. The actin bundles co-localized with the PSD condensates gradually became thicker and longer (Figure 7D; Video S5). Phalloidin staining confirmed that the fluorescence signals of actin represent bundled actin filaments (Figure 7E). Without adding the five PSD components but with the presence of cortactin, Arp2/3 complex, and G-actin, neither His-NR2B clusters nor actin bundles were observed (Figure S6A). We further showed that the PSD can also promote actin bundle formation on the lipid bilayers when Arp2/3 was removed (Figure S6B) and G-actin can be enriched in 6× PSD droplets (Figure S6C), suggesting that PSD condensates can promote F-actin assembly through enriching G-actin and cortactin.

(C) Zoomed-in images of the dashed yellow box in (B) showing the time-dependent clustering of His-NR2B during the spinodal decomposition. Small yellow arrow heads in images at 10–14 min highlight the clusters that were undergoing fusion process. Scale bar, 2 μm.

(D) Fluorescence intensity line-plots showing that the NR2B underwent from originally evenly diffused state (0 min, blue curve) to clustered state (14 min, red curve) after the addition of the PSD scaffold proteins.

(E) Confocal images showing that in the presence of EDTA no NR2B clusters were formed on the lipid bilayers, but instead spherical shaped small droplets were observed in solution.

(F) Co-localization of the PSD scaffold proteins with the NR2B clusters on lipid bilayers (GKAP and SynGAP were not labeled and thus invisible).

(G) FRAP analysis showing the dynamic nature of PSD clusters on lipid bilayers as both Shank3 and SynGAP rapidly exchanged with their counterparts in the dilute phase. The FRAP curves represent averaged results from 20 bleached regions with a squared-shape size of 7.6 μm^2. Data were presented as mean ± SD.

(H) Representative images showing that NR2B failed to be clustered when any one of the four scaffold proteins (PSD-95, GKAP, Shank3, and Homer3) was dropped out from the assay. The clustering of NR2B did not appear to change when SynGAP was omitted. In this assay, only His-NR2B was Cy3-labeled.

The starting concentration of the proteins in solutions (PSD-95, GKAP, Shank3, Homer3, and SynGAP) was at 2 μM each. Cy3-labeled His-NR2B:unlabeled His-NR2B was at 2:100. Experiments were performed in room temperature.

See also Figure S4.

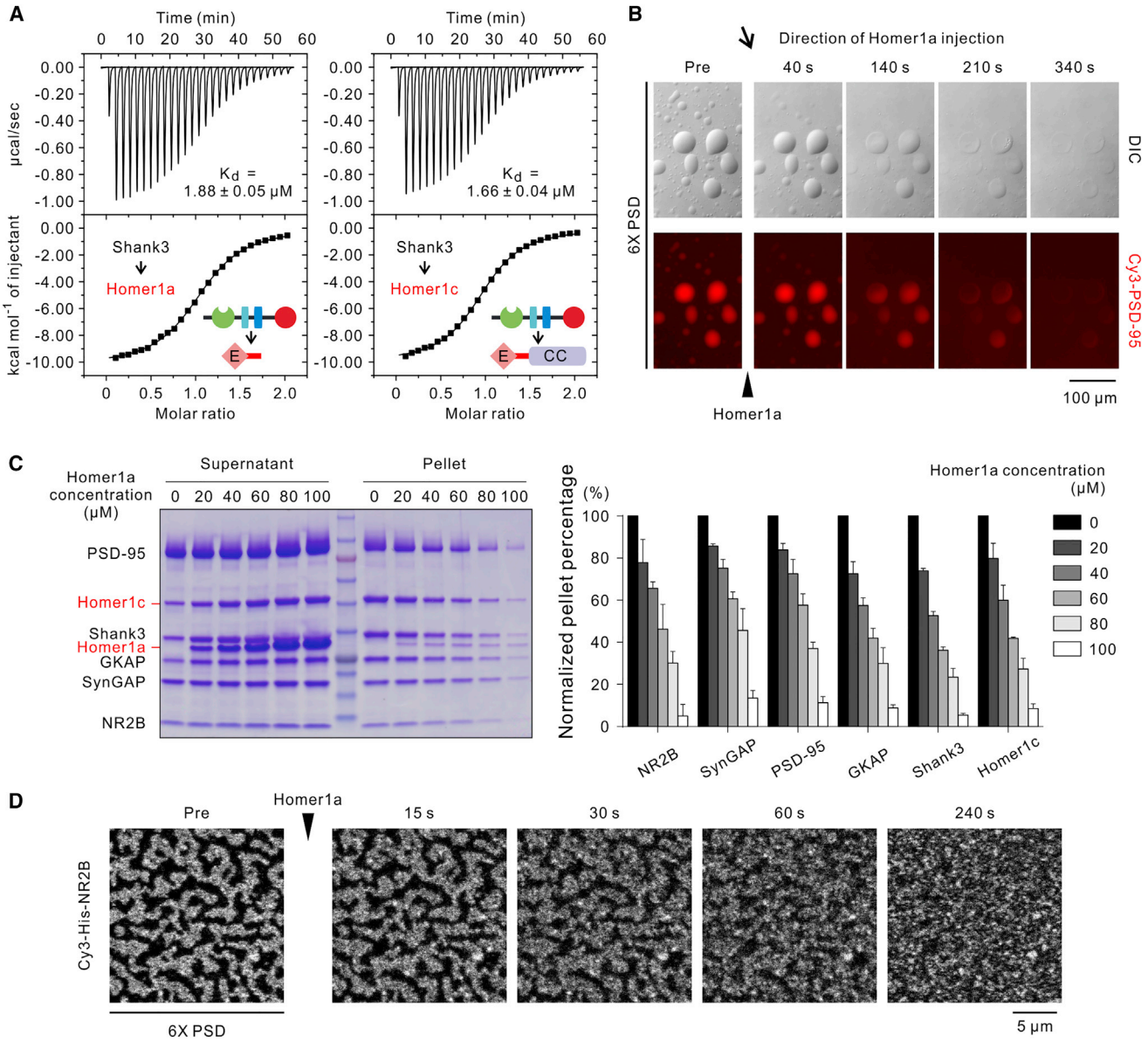

Figure 6. Homer1a Can Globally Scale down PSD Condensates Formation

(A) ITC-based measurement comparing Shank3 binding to Homer1a and Homer1c. Shank3 at 300 μM was titrated into Homer1a or Homer1c at 30 μM in the cell.

(B) Time-lapse DIC and fluorescence images showing that spherical droplets in solution gradually diminished and Cy3-labeled PSD-95 dispersed back to aqueous solution after the injection of purified Homer1a into the chamber. The direction of injection was indicated with an arrow. Related to Video S3.

(C) Sedimentation assay showing that Homer1a prevented the PSD condensates formation in a dose-dependent manner. Indicated concentrations of Homer1a were added into the 6× PSD mixture with each component at the 20 μM concentration. Pellets recovered under the condition without Homer1a were normalized to 100%. Data are presented as mean ± SD with results from 3 independent batches of sedimentation experiments.

(D) Time-lapse confocal images showing that PSD condensates on lipid bilayers dissolved after addition of purified Homre1a. In this 6× PSD de-clustering assay, only His-NR2B was Cy3-labeled and the PSD condensates were pre-formed as indicated in Figure 5B. Related to Video S4.

See also Figure S5.

Reconstituted PSD Condensates Repel Inhibitory Postsynaptic Protein

Finally, we asked whether the reconstituted PSD condensates are driven by a specific mechanism for building up a functional synaptic assembly or a non-specific protein concentration phenomenon capable of gathering any proteins.

The PSD protein condensates should allow small and non-interacting proteins to diffuse in and out freely. We first assayed thioredoxin (TRX), a synapse unrelated protein, on its possible enrichment in PSD condensate. When included at a doubled concentration as the rest of the 6× PSD components, a faint band of TRX existed in the condensed phase (Figure S7A).

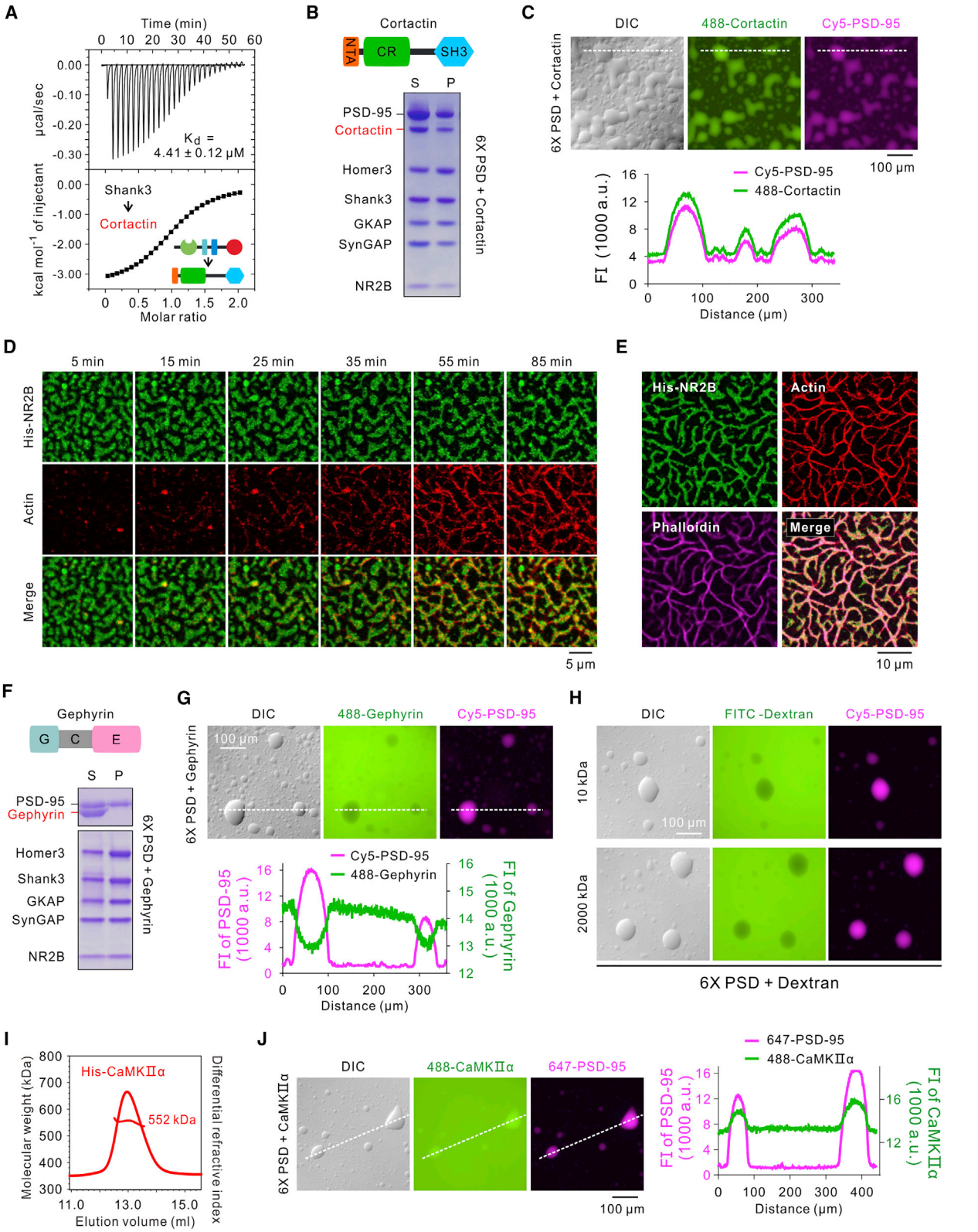

(legend on next page)

Fluorescence imaging-based assay also showed that the PSD condensates is permeable to TRX (Figure S7B). We next investigated the distribution of gephyrin, a master scaffold protein of inhibitory PSDs capable of forming homo-oligomers by itself (Tyagarajan and Fritschy, 2014). Very interestingly, full-length gephyrin showed no condensed phase enrichment at all in the 6× PSD system (Figure 7F), suggesting that it is actively excluded by the 6× PSD condensates. We investigated this possibility further using fluorescence microscopy. It was striking to observe that gephyrin was indeed excluded from the condensed 6× PSD droplets (Figure 7G). It is further noted that such mutual exclusion appeared to only occur in the condensed PSD assembly, as gephyrin and the six excitatory PSD proteins in the dilute phase inter-mixed homogenously (Figure 7G).

A trivial explanation for the gephyrin exclusion from the 6× PSD condensates is that the matrix pore of the 6× PSD network in the condensed phase is too small for gephyrin to enter. To test this possibility, we used a series of FITC-labeled dextran with different molecular weights (10–2,000 kDa). We found by surprise that all forms of dextrans were excluded from the droplets (Figures 7H and S7C), likely due to the highly hydrophilic nature of dextrans. We then used a major excitatory PSD component CaMKIIα for subsequent study. Purified CaMKIIα holoenzyme exists as a dodecamer (Figure 7I). It does not directly interact with any of the six PSD components and thus serves as a "client" to the system. We found that the PSD condensates is also permeable to CaMKIIα (Figure 7J), indicating that the 6× PSD droplet pore size is larger than the diameter of the CaMKIIα holoenzyme. The above data indicate that the exclusion of gephyrin from the 6× PSD condensates is due to the specific molecular features of gephyrin.

DISCUSSION

Via a biochemical reconstitution approach, we have demonstrated here that four major scaffold proteins (PSD-95, GKAP, Shank, and Homer) can form PSD protein condensates at physiological concentrations. The results indicate that the highly condensed PSD assemblies in living neurons might autonomously form and stably exist via LLPS. It provides a likely answer to the mechanism of synapse-based cellular compartmentalization of neurons, a striking morphology that is critical for the functions of neurons. Because the reconstituted PSD condensates are simple and chemically defined, the system could be used to investigate the roles of other PSD proteins in regulating PSD assembly formation and dynamics. The information derived from such a reconstitution system, when combined with experiments performed in living neurons, may offer valuable insights in understanding roles of these proteins in synaptic formation and functions. Additionally, given that a very large proportion of brain disorders may be caused by mutations on genes encoding synaptic proteins, the reconstitution system may also be attractive in investigating how such mutations may alter PSD structure and function.

We observed that the ePSD condensates selectively expel inhibitory postsynaptic (iPSD) scaffold protein gephyrin from entering the condensates. This observation may have implications in understanding the mutual exclusive organization of excitatory and inhibitory synapses on dendrites. A large proportion of inhibitory synapses are localized on dendritic spines (Kubota et al., 2007; Villa et al., 2016). Among those inhibitory synapses, a considerable proportion co-exist with excitatory synapses. However, iPSD and ePSD within a single spine do not inter-mix (Kubota et al., 2007). We speculate that gephyrin and ePSD proteins weakly repel each other. Such weak repulsion forces, when manifested in the highly concentrated condensed phase, causes active exclusion of gephyrin. Such active exclusion of one type of molecule(s) from another functionally distinct type of molecular assembly via formation of biological condensates highlights important roles of weak repulsions in organizing specific functional compartments in living cells.

In summary, the *in vitro* reconstituted ePSD condensates studied here recapture many of the hallmark features observed for these major postsynaptic scaffold proteins in organizing

Figure 7. Reconstituted PSD Condensates Promote Actin Polymerization and Repel Gephyrin

(A) ITC-based measurement showing the binding between cortactin and Shank3. Shank3 at 400 μM was titrated into cortactin at 40 μM in the cell.

(B) Sedimentation assay showing the S/P distribution of cortactin (10 μM) in the 6× PSD (with each component at 30 μM).

(C) DIC and fluorescence images showing that cortactin (10 μM) was recruited to the 6× PSD condensed droplets (with each component at 20 μM). Cortactin and PSD-95 were labeled by Alexa 488 and Cy5, respectively. The rest of the proteins were not labeled. Fluorescence intensities along the dashed line are plotted.

(D) Time-lapse images showing that PSD condensates (indicated by Alexa 488-labeled His-NR2B) on lipid bilayers promoted actin (5% Rhodamine-labeled) polymerization. Time points indicate the time after the rest of 5 unlabeled PSD components (2 μM) together with G-actin (0.5 μM), cortactin (0.2 μM), and Arp2/3 complex (0.03 μM) were added to the NR2B-anchored lipid membrane bilayers. Related to Video S5.

(E) Co-localization of the bundled F-actin with NR2B cluster and the PSD condensates. Bundled F-actin were stained by Alexa 633-phalloidin, and actin was labeled with Rhodamine as in (D). Images were acquired at ~100 min after addition of PSD proteins as indicated in (D).

(F) Sedimentation assay showing that gephyrin (20 μM) was not recovered in the pellet fraction in the 6× PSD (20 μM) phase transition assay. To maximize the resolution, PSD-95 and gephyrin were resolved by 8% SDS-PAGE, and the rest of the proteins were resolved by 4%–15% gradient SDS-PAGE.

(G) DIC and fluorescence images showing that gephyrin (20 μM) was excluded from the 6× PSD (20 μM) condensed droplets. Instead, gephyrin was evenly distributed in the dilute phase. Gephyrin and PSD-95 were labeled by Alexa 488 and Cy5, respectively. Other proteins were unlabeled. Fluorescence intensities along the dashed lines are plotted below.

(H) Both 10 kDa and 2,000 kDa dextrans were excluded by the 6× PSD droplets. 2 μM FITC-labeled dextrans were added to 6× PSD mixtures (20 μM, only PSD-95 was labeled by Cy5). Droplet morphologies were captured by DIC imaging.

(I) FPLC-coupled static light scattering analysis showing the column behavior and detected molecular weight of the purified CaMKIIα holoenzyme. 25 μM purified CaMKIIα holoenzyme was loaded to a Superose 6 size-exclusion column.

(J) PSD condensates are permeable to and can slightly enrich CaMKIIα holoenzyme. 10 μM Alexa 488-labeled CaMKIIα holoenzyme was added to 6× PSD mixtures (20 μM, only PSD-95 was labeled by Alexa 647). Fluorescence intensities along the dashed lines are analyzed at right.

See also Figures S6 and S7.

synaptic signaling complex, promoting synaptic development and maturation, and regulating synaptic plasticity. Although still vastly simplified, this well-defined biochemically traceable system provides a platform and a new paradigm for studying excitatory PSD formation and regulation as well as for elucidating mechanisms of a range of brain disorders caused by mutations of synaptic genes in the future. In a broader sense, principles and mechanisms revealed in the reconstituted PSD condensates here, together with methods developed in this work, may also be applied to other biomolecular condensates.

STAR★METHODS

Detailed methods are provided in the online version of this paper and include the following:

- KEY RESOURCES TABLE
- CONTACT FOR REAGENT AND RESOURCE SHARING
- EXPERIMENTAL MODEL AND SUBJECT DETAILS
  - Bacterial strain
- METHODS DETAILS
  - Protein expression and purification
  - Protein fluorescence labeling
  - Phase transition sedimentation and imaging assay
  - Quantification of protein concentration in the condensed phase
  - Lipid bilayer preparation and phase transition assay
  - Actin polymerization on lipid bilayers
  - Fluorescence recovery after photobleaching (FRAP) assay
  - Atomic force microscopy (AFM) assay
  - Isothermal titration calorimetry (ITC) assay
  - Fast protein liquid chromatography coupled with static light scattering (FPLC-SLS) assay
- QUANTIFICATION AND STATISTICAL ANALYSIS

SUPPLEMENTAL INFORMATION

Supplemental Information includes seven figures and five videos and can be found with this article online at https://doi.org/10.1016/j.cell.2018.06.047.

ACKNOWLEDGMENTS

This work was supported by grants from Research Grant Council (RGC) of Hong Kong (AoE-M09-12 and C6004-17G), a 973 program grant from the Minister of Science and Technology of China (2014CB910204), and a Shenzhen Basic Research grant (JCYJ20160229153100269) to M. Zhang, and grants from RGC of Hong Kong (AoE/P-02/12 and C6004-14G) to P.T. M. Zhang is a Kerry Holdings Professor in Science and a Senior Fellow of IAS at HKUST.

AUTHOR CONTRIBUTIONS

M. Zeng, X.C., D.G., J.X., and H.W. performed experiments. M. Zeng, X.C., D.G., J.X., H.W., P.T., and M. Zhang analyzed data. M. Zeng, X.C., and M. Zhang designed the research. M. Zeng, X.C., and M. Zhang drafted the paper. All authors commented the paper. M. Zhang coordinated the project.

DECLARATION OF INTERESTS

The authors declare no competing interests.

Received: February 8, 2018
Revised: May 17, 2018
Accepted: June 26, 2018
Published: August 2, 2018

REFERENCES

Alberti, S. (2017). The wisdom of crowds: regulating cell function through condensed states of living matter. J. Cell Sci. *130*, 2789–2796.

Araki, Y., Zeng, M., Zhang, M., and Huganir, R.L. (2015). Rapid dispersion of SynGAP from synaptic spines triggers AMPA receptor insertion and spine enlargement during LTP. Neuron *85*, 173–189.

Banani, S.F., Lee, H.O., Hyman, A.A., and Rosen, M.K. (2017). Biomolecular condensates: organizers of cellular biochemistry. Nat. Rev. Mol. Cell Biol. *18*, 285–298.

Banjade, S., and Rosen, M.K. (2014). Phase transitions of multivalent proteins can promote clustering of membrane receptors. eLife *3*. https://doi.org/10.7554/eLife.04123.

Baron, M.K., Boeckers, T.M., Vaida, B., Faham, S., Gingery, M., Sawaya, M.R., Salyer, D., Gundelfinger, E.D., and Bowie, J.U. (2006). An architectural framework that may lie at the core of the postsynaptic density. Science *311*, 531–535.

Bartol, T.M., Bromer, C., Kinney, J., Chirillo, M.A., Bourne, J.N., Harris, K.M., and Sejnowski, T.J. (2015). Nanoconnectomic upper bound on the variability of synaptic plasticity. eLife *4*, e10778.

Brangwynne, C.P., Eckmann, C.R., Courson, D.S., Rybarska, A., Hoege, C., Gharakhani, J., Jülicher, F., and Hyman, A.A. (2009). Germline P granules are liquid droplets that localize by controlled dissolution/condensation. Science *324*, 1729–1732.

Cheng, D., Hoogenraad, C.C., Rush, J., Ramm, E., Schlager, M.A., Duong, D.M., Xu, P., Wijayawardana, S.R., Hanfelt, J., Nakagawa, T., et al. (2006). Relative and absolute quantification of postsynaptic density proteome isolated from rat forebrain and cerebellum. Mol. Cell. Proteomics *5*, 1158–1170.

Cohen, R.S., Blomberg, F., Berzins, K., and Siekevitz, P. (1977). The structure of postsynaptic densities isolated from dog cerebral cortex. I. Overall morphology and protein composition. J. Cell Biol. *74*, 181–203.

de Vivo, L., Bellesi, M., Marshall, W., Bushong, E.A., Ellisman, M.H., Tononi, G., and Cirelli, C. (2017). Ultrastructural evidence for synaptic scaling across the wake/sleep cycle. Science *355*, 507–510.

Diering, G.H., Nirujogi, R.S., Roth, R.H., Worley, P.F., Pandey, A., and Huganir, R.L. (2017). Homer1a drives homeostatic scaling-down of excitatory synapses during sleep. Science *355*, 511–515.

Dosemeci, A., Weinberg, R.J., Reese, T.S., and Tao-Cheng, J.H. (2016). The postsynaptic density: there is more than meets the eye. Front. Synaptic Neurosci. *8*, 23.

Feric, M., Vaidya, N., Harmon, T.S., Mitrea, D.M., Zhu, L., Richardson, T.M., Kriwacki, R.W., Pappu, R.V., and Brangwynne, C.P. (2016). Coexisting liquid phases underlie nucleolar subcompartments. Cell *165*, 1686–1697.

Guan, D., Hang, Z.H., Marcet, Z., Liu, H., Kravchenko, I.I., Chan, C.T., Chan, H.B., and Tong, P. (2015). Direct measurement of optical force induced by near-field plasmonic cavity using dynamic mode AFM. Sci. Rep. *5*, 16216.

Han, K., Holder, J.L., Jr., Schaaf, C.P., Lu, H., Chen, H., Kang, H., Tang, J., Wu, Z., Hao, S., Cheung, S.W., et al. (2013). SHANK3 overexpression causes manic-like behaviour with unique pharmacogenetic properties. Nature *503*, 72–77.

Harbury, P.B., Zhang, T., Kim, P.S., and Alber, T. (1993). A switch between two-, three-, and four-stranded coiled coils in GCN4 leucine zipper mutants. Science *262*, 1401–1407.

Harris, K.M., and Stevens, J.K. (1989). Dendritic spines of CA 1 pyramidal cells in the rat hippocampus: serial electron microscopy with reference to their biophysical characteristics. J. Neurosci. *9*, 2982–2997.

Harris, K.M., and Weinberg, R.J. (2012). Ultrastructure of synapses in the mammalian brain. Cold Spring Harb. Perspect. Biol. *4* https://doi.org/10.1101/cshperspect.a005587.

Hayashi, M.K., Ames, H.M., and Hayashi, Y. (2006). Tetrameric hub structure of postsynaptic scaffolding protein homer. J. Neurosci. *26*, 8492–8501.

Hayashi, M.K., Tang, C., Verpelli, C., Narayanan, R., Stearns, M.H., Xu, R.M., Li, H., Sala, C., and Hayashi, Y. (2009). The postsynaptic density proteins Homer and Shank form a polymeric network structure. Cell *137*, 159–171.

Kim, E., Naisbitt, S., Hsueh, Y.P., Rao, A., Rothschild, A., Craig, A.M., and Sheng, M. (1997). GKAP, a novel synaptic protein that interacts with the guanylate kinase-like domain of the PSD-95/SAP90 family of channel clustering molecules. J. Cell Biol. *136*, 669–678.

Kollmannsberger, P., and Fabry, B. (2011). Linear and nonlinear rheology of living cells. Annu. Rev. Mater. Res. *41*, 75–97.

Kubota, Y., Hatada, S., Kondo, S., Karube, F., and Kawaguchi, Y. (2007). Neocortical inhibitory terminals innervate dendritic spines targeted by thalamocortical afferents. J. Neurosci. *27*, 1139–1150.

Kuznetsova, T.G., Starodubtseva, M.N., Yegorenkov, N.I., Chizhik, S.A., and Zhdanov, R.I. (2007). Atomic force microscopy probing of cell elasticity. Micron *38*, 824–833.

Lü, W., Du, J., Goehring, A., and Gouaux, E. (2017). Cryo-EM structures of the triheteromeric NMDA receptor and its allosteric modulation. Science *355*, eaal3729.

Matsuzaki, M., Ellis-Davies, G.C., Nemoto, T., Miyashita, Y., Iino, M., and Kasai, H. (2001). Dendritic spine geometry is critical for AMPA receptor expression in hippocampal CA1 pyramidal neurons. Nat. Neurosci. *4*, 1086–1092.

Matsuzaki, M., Honkura, N., Ellis-Davies, G.C., and Kasai, H. (2004). Structural basis of long-term potentiation in single dendritic spines. Nature *429*, 761–766.

Naisbitt, S., Kim, E., Tu, J.C., Xiao, B., Sala, C., Valtschanoff, J., Weinberg, R.J., Worley, P.F., and Sheng, M. (1999). Shank, a novel family of postsynaptic density proteins that binds to the NMDA receptor/PSD-95/GKAP complex and cortactin. Neuron *23*, 569–582.

Nishiyama, J., and Yasuda, R. (2015). Biochemical computation for spine structural plasticity. Neuron *87*, 63–75.

Palay, S.L. (1956). Synapses in the central nervous system. J. Biophys. Biochem. Cytol. *2* (4, Suppl), 193–202.

Petersen, J.D., Chen, X., Vinade, L., Dosemeci, A., Lisman, J.E., and Reese, T.S. (2003). Distribution of postsynaptic density (PSD)-95 and Ca2+/calmodulin-dependent protein kinase II at the PSD. J. Neurosci. *23*, 11270–11278.

Petralia, R.S., Sans, N., Wang, Y.X., and Wenthold, R.J. (2005). Ontogeny of postsynaptic density proteins at glutamatergic synapses. Mol. Cell. Neurosci. *29*, 436–452.

Sala, C., Futai, K., Yamamoto, K., Worley, P.F., Hayashi, Y., and Sheng, M. (2003). Inhibition of dendritic spine morphogenesis and synaptic transmission by activity-inducible protein Homer1a. J. Neurosci. *23*, 6327–6337.

Shen, Y., Guan, D., Serien, D., Takeuchi, S., Tong, P., Yobas, L., and Huang, P. (2017). Mechanical characterization of microengineered epithelial cysts by using atomic force microscopy. Biophys. J. *112*, 398–409.

Shin, Y., and Brangwynne, C.P. (2017). Liquid phase condensation in cell physiology and disease. Science *357*, eaaf4382.

Su, X., Ditlev, J.A., Hui, E., Xing, W., Banjade, S., Okrut, J., King, D.S., Taunton, J., Rosen, M.K., and Vale, R.D. (2016). Phase separation of signaling molecules promotes T cell receptor signal transduction. Science *352*, 595–599.

Sugiyama, Y., Kawabata, I., Sobue, K., and Okabe, S. (2005). Determination of absolute protein numbers in single synapses by a GFP-based calibration technique. Nat. Methods *2*, 677–684.

Tyagarajan, S.K., and Fritschy, J.M. (2014). Gephyrin: a master regulator of neuronal function? Nat. Rev. Neurosci. *15*, 141–156.

Valtschanoff, J.G., and Weinberg, R.J. (2001). Laminar organization of the NMDA receptor complex within the postsynaptic density. J. Neurosci. *21*, 1211–1217.

Villa, K.L., Berry, K.P., Subramanian, J., Cha, J.W., Oh, W.C., Kwon, H.B., Kubota, Y., So, P.T., and Nedivi, E. (2016). Inhibitory synapses are repeatedly assembled and removed at persistent sites in vivo. Neuron *89*, 756–769.

Weed, S.A., Karginov, A.V., Schafer, D.A., Weaver, A.M., Kinley, A.W., Cooper, J.A., and Parsons, J.T. (2000). Cortactin localization to sites of actin assembly in lamellipodia requires interactions with F-actin and the Arp2/3 complex. J. Cell Biol. *151*, 29–40.

Welch, J.M., Lu, J., Rodriguiz, R.M., Trotta, N.C., Peca, J., Ding, J.D., Feliciano, C., Chen, M., Adams, J.P., Luo, J., et al. (2007). Cortico-striatal synaptic defects and OCD-like behaviours in Sapap3-mutant mice. Nature *448*, 894–900.

Zeng, M., Shang, Y., Araki, Y., Guo, T., Huganir, R.L., and Zhang, M. (2016a). Phase transition in postsynaptic densities underlies formation of synaptic complexes and synaptic plasticity. Cell *166*, 1163–1175.

Zeng, M., Shang, Y., Guo, T., He, Q., Yung, W.H., Liu, K., and Zhang, M. (2016b). A binding site outside the canonical PDZ domain determines the specific interaction between Shank and SAPAP and their function. Proc. Natl. Acad. Sci. USA *113*, E3081–E3090.

Zeng, M., Ye, F., Xu, J., and Zhang, M. (2018). PDZ ligand binding-induced conformational coupling of the PDZ-SH3-GK tandems in PSD-95 family MAGUKs. J. Mol. Biol. *430*, 69–86.

Zhu, J., Shang, Y., and Zhang, M. (2016). Mechanistic basis of MAGUK-organized complexes in synaptic development and signalling. Nat. Rev. Neurosci. *17*, 209–223.

Zhu, J., Zhou, Q., Shang, Y., Li, H., Peng, M., Ke, X., Weng, Z., Zhang, R., Huang, X., Li, S.S.C., et al. (2017). Synaptic targeting and function of SAPAPs mediated by phosphorylation-dependent binding to PSD-95 MAGUKs. Cell Rep. *21*, 3781–3793.

Please cite this article in press as: Zeng et al., Reconstituted Postsynaptic Density as a Molecular Platform for Understanding Synapse Formation and Plasticity, Cell (2018), https://doi.org/10.1016/j.cell.2018.06.047

STAR★METHODS

KEY RESOURCES TABLE

REAGENT or RESOURCE	SOURCE	IDENTIFIER
Chemicals, Peptides, and Recombinant Proteins		
Recombinant protein: PSD-95 Full length WT (aa 1M-724L, UniProt: P78352-1)	This paper	N/A (custom-made)
Recombinant protein: PSD-95 PDZ 1-2 WT (aa 60E-247S, UniProt: P78352-1)	This paper	N/A (custom-made)
Recombinant protein: PSD-95 PDZ3-SH3-GK WT (aa 309R-724L, UniProt: P78352-1)	Zeng et al., 2016a	N/A (custom-made)
Recombinant protein: PSD-95 SH3-GK WT (aa 422S-724L, UniProt: P78352-1)	This paper	N/A (custom-made)
Recombinant protein: GKAP 3GBR-CT WT (aa 328Q-421S + 916Q-992L, UniProt: Q9D415-1)	This paper	N/A (custom-made)
Recombinant protein: GKAP 3GBR-CT d15 (aa 328Q-421S + 916Q-977S, UniProt: Q9D415-1)	This paper	N/A (custom-made)
Recombinant protein: Shank3 NPDZ-HBS-CBS-SAM M1718E (aa 533D-665R + 1294D-1323P + 1400A-1426P + 1654G-1730S, M1718E,UniProt: Q4ACU6-1)	This paper	N/A (custom-made)
Recombinant protein: SynGAP CC-PBM WT (aa 1147A-1308V, lacking 1192V-1193K and 1293E-1295G, UniProt: J3QQ18-1)	Zeng et al., 2016a	N/A (custom-made)
Recombinant protein: SynGAP CC-PBM LD&KD (aa 1147A-1308V, lacking 1192V-1193K and 1293E-1295G, L1202D & K1252D, UniProt: J3QQ18-1)	Zeng et al., 2016a	N/A (custom-made)
Recombinant protein: SynGAP CC- d4 (aa 1147A-1304Q, lacking 1192V-1193K and 1293E-1295G, UniProt: J3QQ18-1)	Zeng et al., 2016a	N/A (custom-made)
Homer3 EVH1-CC WT (aa 1M-361P, Ser342 is an Arg, UniProt: Q9NSC5-1)	This paper	N/A (custom-made)
Homer3 EVH1-CC LR&LE (aa 1M-361P, Ser342 is an Arg, L338R & L343E UniProt: Q9NSC5-1)	This paper	N/A (custom-made)
Homer1a EVH1-linker WT (aa 1M-186K, UniProt: Q9Z214-3)	This paper	N/A (custom-made)
Homer1a EVH1-linker W-A (aa 1M-186K, W24A, UniProt: Q9Z214-3)	This paper	N/A (custom-made)
Homer1a EVH1-dCT (aa 1M-118Q, UniProt: Q9Z214-3)	This paper	N/A (custom-made)
Homer1c EVH1-CC WT (aa 1M-366S, UniProt: Q9Z214-1)	This paper	N/A (custom-made)
GCN4-NR2B_last 5aa (aa WARMKQIEDKLEE ILSKLYHIENELARIKKLLGSIESDV*)	This paper	N/A (custom-made)
TRX-His-GCN4-NR2B (The above protein with an N-terminal "TRX-His-TEV" tag)	This paper	N/A (custom-made)
Cortactin full length (without repeats 5&6) (aa 1M-472Q, NCBI: NP_001344045)	This paper	N/A (custom-made)
Gephyrin full length (aa 1M-736L UniProt: Q03555-6)	This paper	N/A (custom-made)
Thioredoxin 1 full length (aa 1M-109A, UniProt: P0AA30-1)	This paper	N/A (custom-made)
CaMKIIα full length (aa 1M-478H, UniProt:P11275-1)	This paper	N/A (custom-made)
G-Actin	Cytoskeleton	Cat#AKL99
Rhodamine G-Actin	Cytoskeleton	Cat#AR05
Arp2/3 complex	Cytoskeleton	Cat# RP01P-A
Alexa Fluor 647 Phalloidin	Invitrogen	Cat#A22287

(*Continued on next page*)

Continued

REAGENT or RESOURCE	SOURCE	IDENTIFIER
iFluor 405 succinimidyl ester	AAT Bioquest	Cat#1021
Alexa Fluor 488 succinimidyl ester	ThermoFisher	Cat#A20000
Cy3 monosuccinimidyl ester	AAT Bioquest	Cat#271
Cy5 monosuccinimidyl ester	AAT Bioquest	Cat#151
Alexa Fluor 647 carboxylic acid, succinimidyl ester	Invitrogen	Cat#A20006
POPC	Avanti	Cat#850457P
DGS-NTA(Ni)	Avanti	Cat#790404P
PEG5000 PE	Avanti	Cat#880230P
FITC-Dextran 10kD	Sigma	Cat#SLBT4519
FITC-Dextran 40kD	Sigma	Cat#SLBT8690
FITC-Dextran 70kD	Sigma	Cat#SLBT8689
FITC-Dextran 150kD	Sigma	Cat#3BCBV3832
FITC-Dextran 250kD	Sigma	Cat#SLBR7368V
FITC-Dextran 500kD	Sigma	Cat#SLBR9842V
FITC-Dextran 2000kD	Sigma	Cat#SLBW1874
Gradient SDS-PAGE gel	BioRad	Cat#4561096
Experimental Models: Organisms/Strains		
Escherichia coli BL21 (DE3) cells	Invitrogen	Cat# C600003
Recombinant DNA		
Plasmid: 32M3C-PSD95 FL	This paper	N/A
Plasmid: 32M3C-PSD95 PDZ1-2	This paper	N/A
Plasmid: 32M3C-PSD95 PDZ3-SH3-GK	Zeng et al., 2016a	N/A
Plasmid: 32M3C-PSD95 SH3-GK	This paper	N/A
Plasmid: 32M3C-GKAP 3GBR-CT	This paper	N/A
Plasmid: 32M3C-GKAP 3GBR-CT d15	This paper	N/A
Plasmid: M3C-Shank3 NPDZ-HBS-CBS-SAM M1718E	This paper	N/A
Plasmid: MG3C-SynGAP CC-PBM WT	Zeng et al., 2016a	N/A
Plasmid: MG3C-SynGAP CC-PBM LD&KD	Zeng et al., 2016a	N/A
Plasmid: MG3C-SynGAP CC-d4	Zeng et al., 2016a	N/A
Plasmid: M3C-Homer 3 EVH1-CC WT	This paper	N/A
Plasmid: M3C-Homer 3 EVH1-CC LR&LE	This paper	N/A
Plasmid: M3C-Homer1a EVH1-linker WT	This paper	N/A
Plasmid: M3C-Homer1a EVH1-linker W-A	This paper	N/A
Plasmid: M3C-Homer1a EVH1-dCT	This paper	N/A
Plasmid: M3C-Homer1c EVH1-CC WT	This paper	N/A
Plasmid: 32M3C-GCN4-NR2B	This paper	N/A
Plasmid: 32MTEV-GCN4-NR2B	This paper	N/A
Plasmid: M3C-Cortactin full length (without repeats 5&6)	This paper	N/A
Plasmid: M3C-Gephyrin full length	This paper	N/A
Plasmid: M3C- CaMKIIα full length	This paper	N/A
Software and Algorithms		
Origin7.0	OriginLab	https://www.originlab.com/
PyMOL	PyMOL	https://pymol.sourceforge.net/
ASTRA6	Wyatt	http://www.wyatt.com/products/software/astra.html
ImageJ	NIH	https://imagej.nih.gov/ij/
Prism	GraphPad	https://www.graphpad.com/scientific-software/prism/
Amino Acid Composition Analysis	This paper	http://qxcai.people.ust.hk/aaca.html

CONTACT FOR REAGENT AND RESOURCE SHARING

Further information and requests for resources and reagents should be directed to and will be fulfilled by the Lead Contact, Mingjie Zhang (mzhang@ust.hk)

EXPERIMENTAL MODEL AND SUBJECT DETAILS

Bacterial strain

Escherichia coli BL21 cells were used in this study for the production of recombinant proteins. Cells were cultured in LB medium supplemented with necessary antibiotics.

METHODS DETAILS

Protein expression and purification

Various proteins were generated using standard PCR-based methods, cloned into vectors containing an N-terminal TRX-His_6/ GB1-His_6/ His_6-affinity tag followed by an HRV 3C or TEV cutting site. Vector sequences were confirmed by DNA sequencing. Recombinant proteins were expressed in *Escherichia coli* BL21 cells in LB medium at 16°C overnight and protein expression was induced by 0.25 mM IPTG (final concentration) at OD_{600} between 0.6-0.8 unless otherwise noted. Recombinant proteins were purified using a nickel-NTA agarose affinity column followed by size-exclusion chromatography (Superdex 200 or Superdex 75 as see fit) with a column buffer containing 50 mM Tris, pH 8.2, 100 mM NaCl, 1 mM EDTA, 2 mM DTT. DNA contamination (e.g., in purification of the full-length PSD-95, Gephyrin, CaMKIIα, and the tetrameric Homer) or protein degradation were further separated by mono Q. CaMKIIα was co-expressed with λ-phosphatase and protein expression was induced by 1 mM IPTG (final concentration) at OD_{600} around 1. 10% glycerol was supplied in all buffers during CaMKIIα purification process. When needed, recombinant protein tags were cleaved by HRV 3C protease and separated by another step of size-exclusion chromatography.

We used the full-length PSD-95 and Homer3 for the reconstitution experiments, as both proteins are highly soluble and do not display concentration-dependent self-association property that would complicate phase transition experiments. To obtain soluble and well behaving GKAP (aka SAPAP1 or DLGAP1) and Shank3, we removed part of the sequences of the two proteins. Specifically, we removed part of the sequences on GKAP connecting three PSD-95 GK-binding repeats (GBRs) (Kim et al., 1997; Zhu et al., 2017) and a C-terminal extended PDZ-binding motif (PBM) required for stable Shank binding (Zeng et al., 2016b). Shank3 is a very large scaffold protein that is difficult to obtain a highly purified, well behaving full-length recombinant protein. Through extensive trials, we found that a simplified Shank3 protein could be obtained in large quantity, which contains an N-terminal extended PDZ domain, a Homer-binding sequence (HBS) and a Cortactin-binding sequence (CBS) in the poly-Pro region, followed by a C-terminal SAM domain mediating self-oligomerization. We further introduced an M1718E mutation in the Shank3 SAM domain to obtain a highly soluble Shank3 protein (Baron et al., 2006). The major SynGAP isoform, SynGAPα1, contains a conserved trimeric coiled-coil (CC) domain and a PSD-95 PDZ3-SH3-GK (P-S-G) tandem-binding PBM. Synaptic localization and activity-dependent dispersion of SynGAPα1 require both its CC domain and PBM (Zeng et al., 2016a). We thus purified the C terminus of SynGAPα1 containing the CC-PBM domain (referred to as SynGAP in the study) for its PSD assembly study. Cares were taken to keep sufficiently long connecting sequences between each protein interaction motif/domain to maintain the conformational flexibility of all of the modified proteins used in this study (Figure 1A).

Protein fluorescence labeling

Highly purified proteins were prepared in $NaHCO_3$ buffer (containing 100 mM $NaHCO_3$, pH 8.3, 100 mM NaCl, 1 mM EDTA and 2 mM DTT) and concentrated to 5-10 mg/ml. Cy3/Cy5/iFluor 405 NHS ester (AAT Bioquest), Alexa 488 NHS ester (ThermoFisher), and Alexa 647 NHS ester (Invitrogen) were dissolved by DMSO and incubated with the corresponding protein at room temperature for 1 hr (fluorophore to protein molar ratio was 1:1). Reaction was quenched by 200 mM Tris, pH 8.3. The fluorophores and other small molecules were removed from the proteins by passing the reaction mixture through a Hitrap desalting column with buffer containing 50 mM Tris, pH 8.2, 100 mM NaCl, 1 mM EDTA, and 2 mM DTT. Fluorescence labeling efficiency was measured by Nanodrop 2000 (ThermoFisher). In imaging assays, fluorescence labeled proteins were further diluted with the corresponding unlabeled proteins in the same buffer. Typically, for components in solution, the final ratio of fluorescence labeled protein: unlabeled protein was 1:100; for His-NR2B on lipid bilayers, the final ratio was 2:100. When labeling CaMKIIα, 10% glycerol was also added in the reaction buffer.

Phase transition sedimentation and imaging assay

Proteins were prepared in buffer containing 50 mM Tris, pH 8.2, 100 mM NaCl, 1 mM EDTA, and 2 mM DTT (with affinity tags cleaved and removed) and pre-cleared via high-speed centrifugations. Proteins were then mixed or diluted with buffer to designed combinations and concentrations.

For sedimentation assay, typically, the final volume of each reaction is 100 μl. After 10 min equilibrium at room temperature, protein samples were subjected to sedimentation at 16,873 g for 10 min at 25°C on a table-top temperature-controlled micro-centrifuge.

After centrifugation, the supernatant and pellet were immediately separated into two tubes. The pellet fraction was thoroughly re-suspended with the same buffer to the equal volume as supernatant fraction (typically, to 100 μl). Proteins from both fractions were analyzed by SDS-PAGE (4%–15% gradient gel if not specifically stated) with Coomassie blue staining. Band intensities were quantified using the ImageJ software.

For imaging assay, protein samples were injected into a homemade flow chamber (comprised of a glass slide sandwiched by a coverslip with one layer of double-sided tape as a spacer) for DIC and fluorescent imaging (Nikon Ni-U upright fluorescence microscope) at room temperature. Glasses were washed by Hellmanex II (Hëlma Analytics) and 2 M NaOH sequentially and thoroughly rinsed with MilliQ H_2O before chamber making. During imaging, the chamber was sealed by nail polish to reduce solution evaporation. Image fluorescence intensities were analyzed by the ImageJ software.

Quantification of protein concentration in the condensed phase

Confocal imaging-based fluorescent intensity measurement of proteins in the condensed droplets

The first step toward absolute concentration measurement of individual components in the 4× and 6× PSD condensates was to determine fluorescence intensities of confocal planes that are completely within the PSD droplets as indicated in Figures 3A and 3B. In each measurement, only one component was Cy3-labeled to avoid any possible signal cross-talk and labeled protein was adjusted to 1% by diluting a labeled protein into the unlabeled one. The 1% Cy3-labeled protein was further mixed with other unlabeled proteins to form 4× or 6× PSD condensates. Samples containing condensed droplets were injected into homemade chamber and imaged by a Zeiss LSM880 confocal microscope with a 63× objective lens in a z stack mode with the step interval as 1.0 μm. Pinhole size was set at 1 Airy unit and the z-dimensional optical section thickness was ~0.9 μm (defined by the full width half maximum of z-dimensional point spread function ($FWHM_z$) using fluorescence beads with diameter of 100 nm). The lowest z-slice started with the focus in the coverslip layer and the highest z-slice ended with the focus entering the dilute solution layer (usually with 8-15 slices dependent on the thickness of droplets). As shown in Figure 3A, the signal intensity in the lowest layer (layer 1) of the droplet is usually lower than the layers above likely because part of the optical section layer overlaps with the coverslip glass. After the optical section layer goes up into the droplet (layers 2-4 in Figure 3A), the fluorescence intensities within the droplet reach the peak values and become more or less constant, indicating that Homer3 distribution within the droplet is homogeneous both in the x-y dimensions and in the z-dimension in these layers. When the optical section layer keeps going up and reaches the top-surface edge of the droplet, the intensity value decreases. For example, the signal intensity for the layer 6 likely reflects the signal summation of part of the droplet and part of the dilute phase solution. For quantification, we define that a z-slice with its peak intensity < 10% deviation from the maximal peak intensity layer (i.e., $(\mathbf{I}_{max}\text{-}\mathbf{I})/\mathbf{I}_{max} < 10\%$) is with its imaging plane entirely within the z-dimension of the droplet (e.g., layers 2-4 in the schematic diagram in Figure 3A and layers 2-7 in Figure 3B). This selection criteria ensured that the point spread function of each selected z-slice was within the height of each droplet (> 5 μm). The fluorescence intensities of these layers were averaged for absolute protein concentration calculation. Identical parameters (including laser power, detector gain, resolution, scanning speed, etc.) were used during the imaging processes. To assure system stability, all measurements, together with the calibration curve, were completed in one single imaging session. Images were analyzed by the ImageJ software.

Absolute protein concentration calculation

To generate a standard calibration curve for directly converting the measured florescence intensity into absolute protein concentration, Cy3-labeled Shank3 at different indicated concentrations (measured by a spectrophotometer as Nanodrop 2000 (ThermoFisher)) were injected into the flow chamber and the fluorescence intensity at each concentration was measured using the same imaging parameters as for the droplet quantifications. With this calibration curve, the measured fluorescence intensity for each component in a given condensed PSD system can be converted into absolute molar concentration.

Lipid bilayer preparation and phase transition assay

Small unilamellar vesicle (SUV) preparation:

Phospholipids containing 98% POPC (Avantilipids), 2% DGS-NTA-Ni (Avantilipids) and 0.1% PEG 5000 PE (Avantilipids) were dried under a stream of nitrogen and resuspended by PBS to a final concentration of 0.5 mg/ml. The lipid solution was repeatedly frozen and thawed using a combination of liquid N_2 and 37°C water bath until the solution turned clear. Then the solution was subjected to a centrifugation at 33,500 g for 45 min at 4°C. Supernatant containing SUVs was collected.

Chambered cover glass wash and lipid coating

Chambered cover glass (Lab-tek) was initially washed with Hellmanex II (Hëlma Analytics) overnight, thoroughly rinsed with MilliQ H_2O. The cover glass was then washed with 5M NaOH for 1 hr at 50°C and thoroughly rinsed with MilliQ H_2O, repeated for three times, and followed by equilibration with the Protein Buffer (50 mM Tris, pH 8.2, 100 mM NaCl, 1 mM TCEP). Typically, 150 μL SUVs were added to a cleaned chamber and incubated for 1 hr at 42°C, allowing SUVs to fully collapse on glass and fuse to form supported lipid bilayers (SLBs). SLBs were washed with the Protein Buffer for three times (6-folds dilution per time, 216-folds dilution in total) to remove extra SUVs. Then it was blocked with the Cluster Buffer (the Protein Buffer supplied with 1 mg/ml BSA) for 30 mins at room temperature.

Lipid bilayer phase transition assay

This supported membrane bilayers were doped with DGS lipid with Ni^{2+}-NTA attached to its head. We used GCN4-NR2B with an N-terminal thioredoxin (TRX)-His_6 tag (referred to as His-NR2B), so that a fluorescence tag (Cy3 or Alexa 488 in this study) can be

added to the N-terminal end of the fusion protein (on the TRX N-terminus) without affecting the His_6-tag from attaching to Ni^{2+}-NTA-DGS embedded in the lipid bilayers (Figure 5A). The thioredoxin-tag also provides a space to separate the chemical fluorophore from the surface of lipid bilayers to avoid potential non-specific interaction between the dye and the membranes. PSD components were prepared in the Protein Buffer. Initially, 4 μM His-NR2B was added and incubated with SLBs for 1 hr at room temperature, followed by washing with the Cluster Buffer for three times to remove unbound His-NR2B. Other PSD components (typically, each at 2 μM) were premixed in the Cluster Buffer and then added to the His-NR2B-bound SLBs, waiting for phase transition to happen on the lipid bilayers. All data were collected within 8 hr after lipid coating started.

Actin polymerization on lipid bilayers

Lipid bilayers and phase transitioned clusters were prepared as above. For actin polymerization assay, 0.5 μM actin (5% Rhodamine labeled) (Cytoskeleton), 0.2 μM purified Cortactin and 0.03 μM Arp2/3 complex (Cytoskeleton) were premixed with other five PSD components with each at 2 μM in the Cluster Buffer supplied with 0.5 mM ATP, 1 mM $MgCl_2$ and 0.03 μM Alexa 633-phalloidin (Invitrogen), and then added into the chamber containing His-NR2B-bound SLBs.

Fluorescence recovery after photobleaching (FRAP) assay

FRAP assay was performed on a Zeiss LSM 880 confocal microscope at 20-25°C. Cy3 signal was bleached using a 561-nm laser beam. Diameters of the bleached droplets/membrane regions were indicated in each figure legend. The fluorescence intensity difference between pre-bleaching and at time 0 (the time point right after photobleaching pulse) was normalized to 100%. The experimental control is to quantify fluorescence intensities of similar droplet/ membrane regions without photobleaching. Except the FRAP assay on aged droplets (Figure S3G), all data were collected within 1 hr after LLPS formation.

Atomic force microscopy (AFM) assay

For mechanical characterization of PSDs, we used an AFM instrument (MFP-3D, Asylum Research) equipped with a colloidal probe. The cantilevers used in the experiment were triangular micro-cantilevers (BL-TR800PB, Asylum Research) featuring a spring constant $k \approx 0.6$ N/m. The colloidal probe was assembled as described previously by adhering a glass sphere of diameter $d \simeq 17.5$ μm to the front end of the cantilever (Guan et al., 2015). The surface of the probe was coated with a thin layer of PLL-g-PEG (SuSoS AG.), which provided a high degree of resistance to protein adsorption in the solution and also reduced adhesion on the PSD surface. Prior to each measurement, we calibrated the *in situ* spring constant *k* of the probe using the thermal power spectral density method (Guan et al., 2015). Protein were prepared in buffer with 50 mM Tris, pH 7.8, 100 mM NaCl, 1 mM EDTA, and 2 mM DTT and with all affinity tags removed. Protein concentrations for 6× PSD droplets were at 5 μM and for 2× PSD droplets were at 100 μM to generate droplets sizes comparable to the 6× PSD system.

The AFM measurements were performed in the contact mode by moving the colloidal probe vertically on the top of the PSD droplet. The z axis piezoelectric actuator of the AFM was controlled to move the probe up or down at a constant speed in the range of 3.5–50 μm/s. AFM measured the force generated by condensed droplets deformation after the probe compressed the droplets. When a target force (~3 nN) was reached, the AFM probe retracted. The measured approach curves were found to be well described by the Hertz model (Kuznetsova et al., 2007; Shen et al., 2017), $\boldsymbol{F} = 4/3\boldsymbol{E}\boldsymbol{R}^{1/2}\boldsymbol{\delta}^{3/2}$, where *E* is the reduced Young's modulus of the material, $R = 1/(1/R1 + 1/R2)$ is the effective radius of the probe $R1 = d/2$ and the droplet *R2*, and δ is the indentation depth. In Figure 2D, the green dashed line shows the validity of the Hertz model for describing the measured approach curves, and the best fitting gives the elastic modulus *E* of the PSDs. Except the AFM assay on aged droplets (Figure S3E), all measurements were performed within 70 mins after mixing the PSD components.

Isothermal titration calorimetry (ITC) assay

ITC measurements were carried out on a Microcal VP-ITC calorimeter at 25°C. Proteins used for ITC measurements were dissolved in an assay buffer composed of 50 mM Tris, pH 8.2, 100 mM NaCl, 1 mM EDTA, and 2 mM DTT. High concentration of protein was loaded into the syringe and titrated into the cell containing low concentration of corresponding interactors (concentrations for each reaction were indicated in the figure legends). For each titration point, a 10 μL aliquot of a protein sample in the syringe was injected into the interacting protein in the cell at a time interval of 2 min. Titration data were analyzed using the Origin7.0 software and fitted with the one-site binding model.

Fast protein liquid chromatography coupled with static light scattering (FPLC-SLS) assay

The analysis was performed on an AKTA FPLC system (GE Healthcare) coupled with a static light scattering detector (miniDawn, Wyatt) and a differential refractive index detector (Optilab, Wyatt). Protein samples (concentrations for each reaction were indicated in the figure legends) were filtered and loaded into a Superose 12 10/300 GL column pre-equilibrated by a column buffer composed of 50 mM Tris, pH 8.2, 100 mM NaCl, 1 mM EDTA, and 2 mM DTT. For CaMKIIα molecular weight detection, the buffer was further supplied with 10% glycerol and a Superose 6 10/300 GL column was used. Data were analyzed with ASTRA6 (Wyatt).

QUANTIFICATION AND STATISTICAL ANALYSIS

Statistical parameters including the definitions and exact values of n (e.g., number of experiments, number of droplets, etc), distributions and deviations are reported in the Figures and corresponding Figure Legends. Data of *in vitro* phase transition sedimentation assay and FRAP assay were expressed as mean ± SD ns, not significant; *, $p < 0.05$; **, $p < 0.01$; ***, $p < 0.001$; ****, $p < 0.0001$ using one-way ANOVA with Dunnett's multiple comparisons test. Statistical analysis was performed in GraphPad Prism.

Supplemental Figures

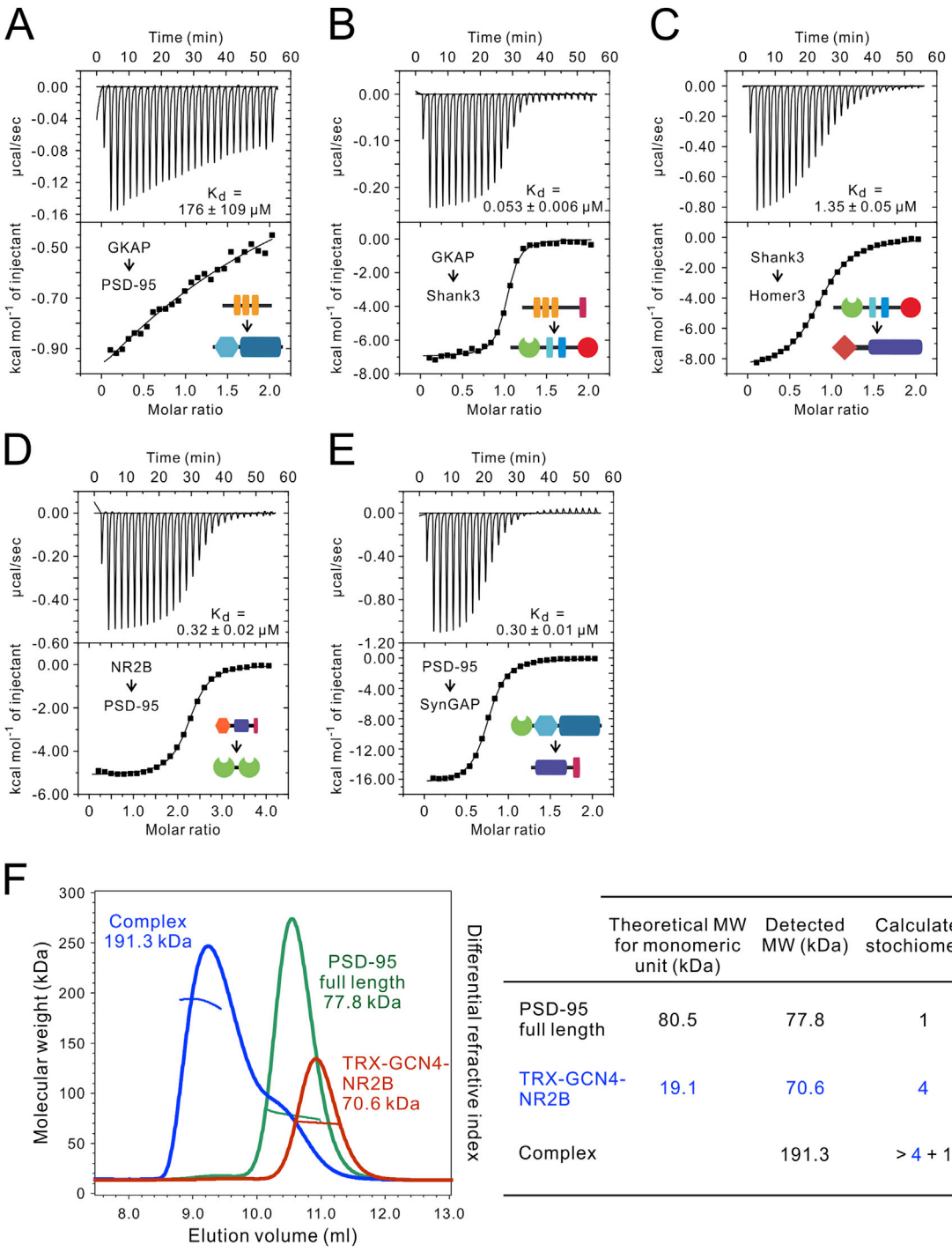

	Theoretical MW for monomeric unit (kDa)	Detected MW (kDa)	Calculated stochiometry
PSD-95 full length	80.5	77.8	1
TRX-GCN4-NR2B	19.1	70.6	4
Complex		191.3	> 4 + 1

Figure S1. ITC- and FPLC-Based Measurements of the Interactions between the PSD Components Used in the Current Study, Related to Figure 1

(A) The N-terminal GK binding repeats (GBR) of GKAP binding to PSD-95 SH3-GK tandem with 500 μM GKAP GBR titrated into 50 μM PSD-95 SH3-GK.

(B) GKAP binding to Shank3 with 100 μM GKAP titrated into 10 μM Shank3.

(C) Shank3 binding to Homer3 with 300 μM Shank3 titrated into 30 μM Homer3.

(D) Tetramerized NR2B binding to PSD-95 with 300 μM TRX-GCN4-NR2B titrated into 15 μM PSD-95 PDZ1-2.

(legend continued on next page)

(E) PSD-95 PDZ3-SH3-GK tandem (P-S-G) binding to SynGAP coiled-coil-PBM trimer (CC-PBM) with 200 μM PSD-95 P-S-G titrated into 20 μM SynGAP CC-PBM.

(F) FPLC-SLS analysis showing that the full-length PSD-95 (50 μM) is a monomer; TRX-GCN4-NR2B (100 μM) is a tetramer; TRX-GCN4-NR2B (100 μM) binding to the full-length PSD-95 (50 μM) induced multimer formation of the PSD-95/ GCN4-NR2B complexes because the detected molecular weight suggests more than one PSD-95 molecules exist in the complex peak.

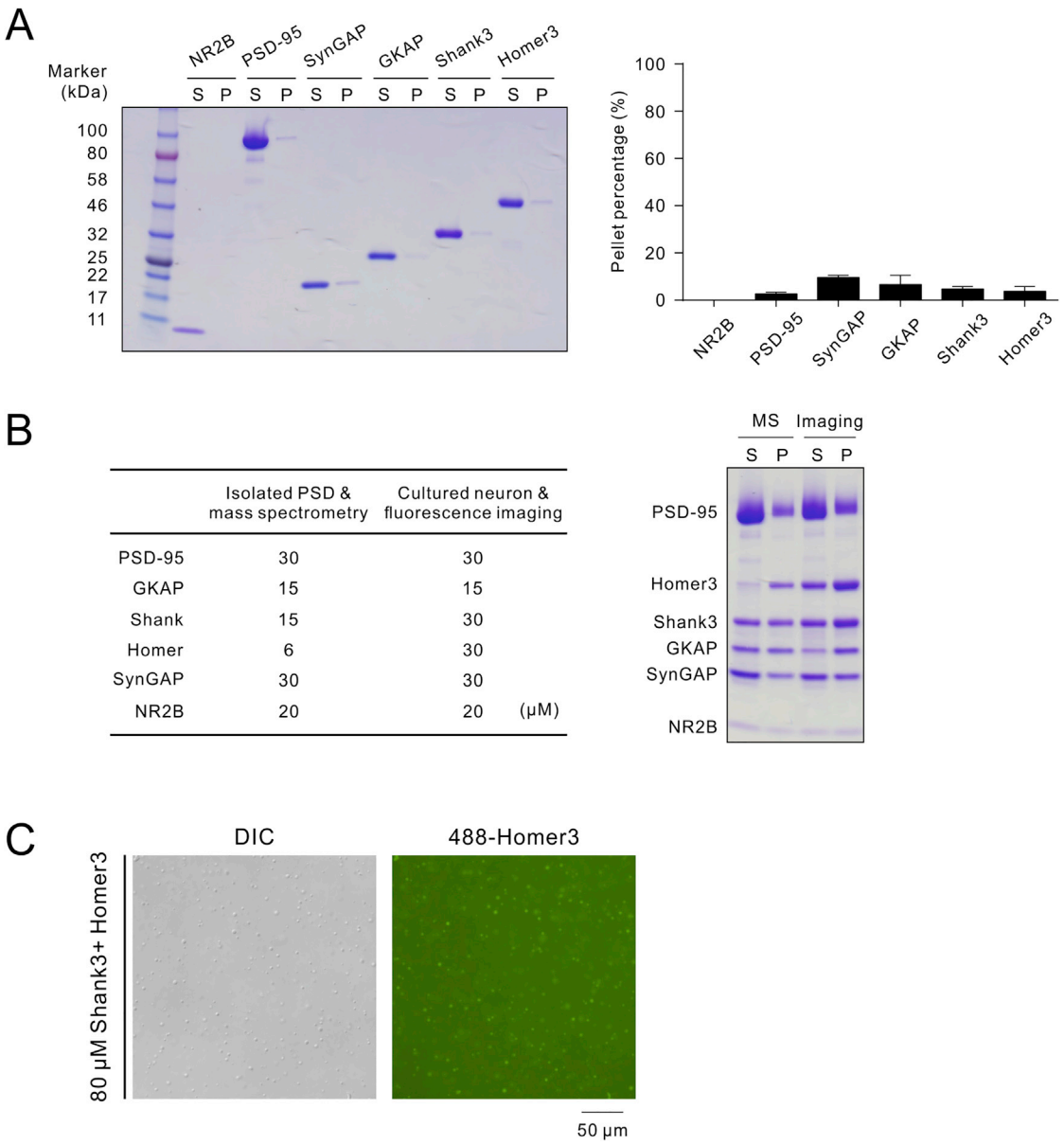

Figure S2. Phase Transition Properties of the 6× PSD System, Related to Figures 1 and 2

(A) Sedimentation assay showing each PSD component alone is highly soluble and does not undergo phase transition. In this assay, the concentration of PSD-95, GKAP, Shank3, Homer3, and SynGAP was each set at 20 μM and NR2B was at 40 μM. Statistic data of the background level of the proteins recovered in the pellet fractions are presented as mean ± SD with results from 3 independent batches of sedimentation experiments.

(B) Comparison of different stoichiometry of the 6× PSD system on their phase transitions by the sedimentation-based assays. (*Left*) The concentrations of the proteins in the two groups are formulated based on the stoichiometry of native PSD calculated by mass spectrometry-based proteomic studies and imaging-based experiments. (*Right*) Sedimentation assay showing the 6× PSD system with different stoichiometry both exhibited phase separations.

(C) A 1:1 mixture of unlabeled Shank3 and 1% Alexa 488-labeled Homer3 at 80 μM underwent phase transition and numerous small spherical droplets were observed by DIC and fluorescence microscopic imaging.

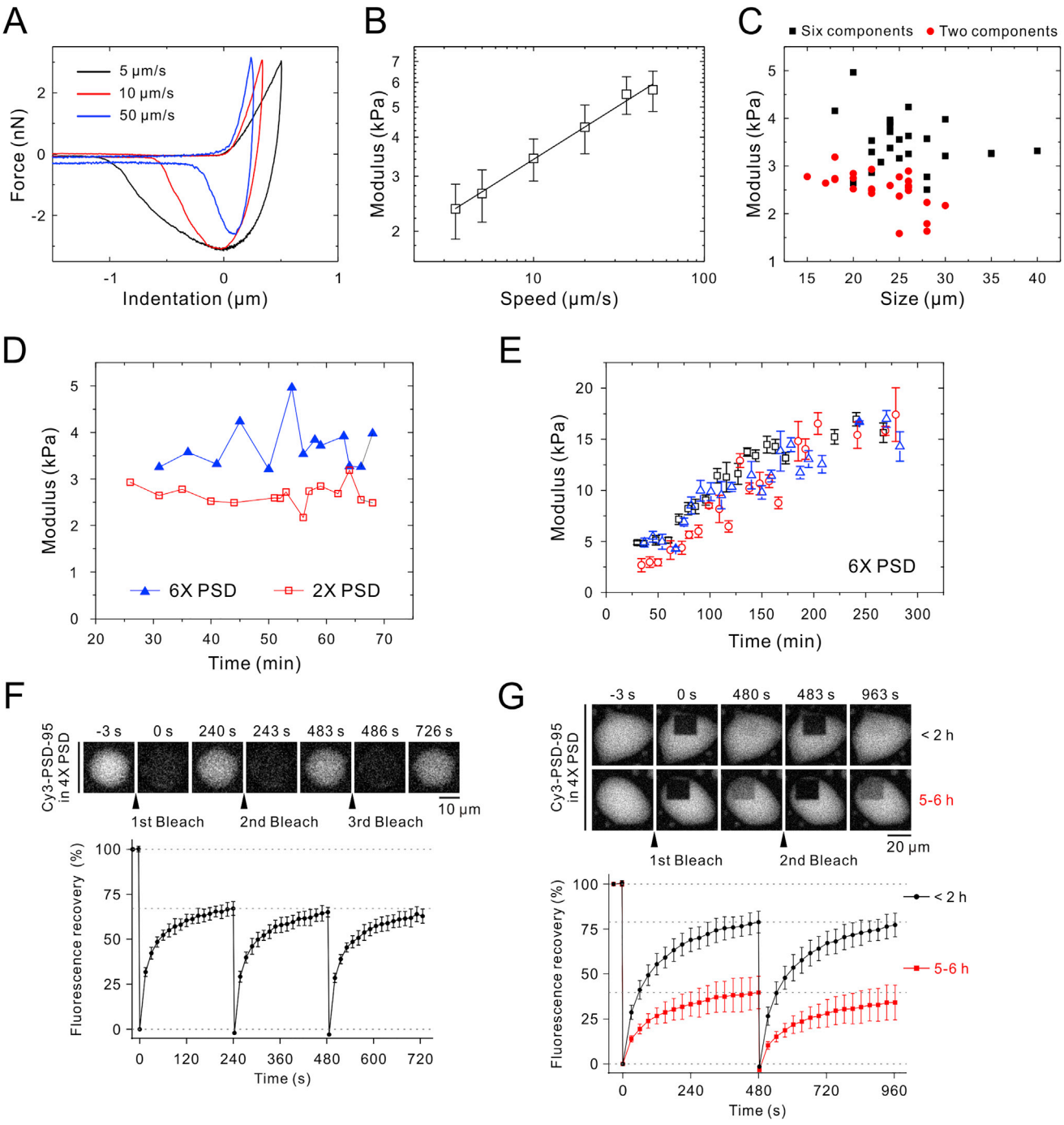

Figure S3. Material Properties of PSD Condensates, Related to Figures 1 and 2

(A) The force-indentation curves measured on the 6× PSD droplets by AFM. The measurements were made when the probe moved downward and upward at a constant speed of 5 μm/s (black), 10 μm/s (red), and 50 μm/s (blue), respectively.

(B) The measured elastic modulus *E* as a function of the indentation speed. The solid line shows the fitting to a power law model with the best fit exponent α = 0.345. 9 droplets were measured for each speed and data are presented as mean ± SD.

(C) The measured elastic modulus *E* of the PSD droplets in different sizes. The size of the PSD droplets is expressed as the apparent diameter of the droplet measured from the top-on view image during the AFM measurements. The plot shows that the measured *E* at the indentation speed of 10 μm/s doesn't depend on the size of the PSD droplets, suggesting the material properties of the PSD condensates do not vary significantly with the size of the droplets.

(D) The distribution of the measured elastic modulus *E* of the PSD droplets in Figure 2E as a function of the time. Time 0 refers to the time point of droplet formation, and the measurements started at 25 min after the experimental setup. The plot shows that the measured *E* doesn't depend on time during the first 70 min during the AFM measurement, suggesting the material properties of the PSD condensates do not vary significantly during the time period.

(legend continued on next page)

(E) The elastic modulus *E* of three different 6× PSD droplets showing a consistent time-dependent hardening over a time period of 5 hr. The symbols in different colors indicate the results of three individual droplets. Each data point represents the average of four measurements, and the error bars are expressed as the standard deviation of the measurements.

(F) FRAP curves of Cy3-PSD-95 in the 4× PSD system from three consecutive photo-bleaches. The top shows the images of a single droplet during the photo-bleach experiment. The curve below represents an averaged signal from 6 droplets with a diameter ~17 μm (as in Figure 1D) and the intensity in each data point is presented as mean ± SD.

(G) Aging of PSD condensates over a long period of time. The Cy3-PSD-95 signal within a 17x17 μm square in a large 4× PSD droplet was bleached twice (with 8 min interval). The portion of more mobile fraction decreased as the droplets were aged for 5-6 hr (black versus red curve). Both curves below represent averaged signals from 5 droplets and are presented as mean ± SD. In both F&G panels, the concentration for each component in 4× PSD droplets was 20 μM as in Figure 1D.

Aging of 6× PSD droplets: Phase separated droplets are known to harden over time, we also measured whether the PSD assembly might also undergo time-dependent aging using AFM. Instead of finishing all of our measurements at a time window between 25-70 min after mixing the PSD proteins (Figure S3D), we measured elasticity of 6× PSD droplets over a 5-hr time span. We found that the 6× PSD droplet has a growth curve-like hardening process (Figure S3E). The elasticity values of the droplets were stable in the first 80 min or so. The elasticity of droplets increased from the initial value of 3.5 ± 1.5 kPa to about 16 ± 3 kPa at the next 120 min time window, and then reached a plateau after 200 min. The Young's modulus increases ~4.5 times over the 5-hr time window, indicating an obvious aging and hardening of the 6× PSD system over the time (Figure S3E).

We have also investigated the droplet aging using FRAP-based imaging method. It was noted that the florescence signal in 4× and 6× PSD droplets did not fully recover after photo-bleaching (Figures 1D and 1G), suggesting there existed a fraction of less mobile components in both systems. To test this possibility, we performed three bleaches in a row to the same 4× PSD droplet. After the first bleach, the recovery curve is similar to Figure 1D, with ~60%–70% recovery after 4 min (Figure S3F). We then immediately performed second and third bleaches and we observed near 100% recovery compared to the first bleach (Figure S3F). This FRAP experiment indicates that the formed PSD droplets contains a mobile fraction and a less mobile fraction. We next examined the formed droplets might undergo aging in a longer time window. We bleached a square in a bigger 4× PSD droplet. For freshly formed droplets (within 2 hr after formation), the fluorescence intensity recovered to ~75% of the initial value after the first bleach and followed by a 100% recovery after the immediate second bleach (Figure S3G). However, for "aged" droplets (5-6 hr after formation), only ~40% fluorescence intensity recovered after the first and the second bleaches (Figure S3G), indicating that a large proportion of materials in the PSD condensates aged over the time window of 5-6 hr.

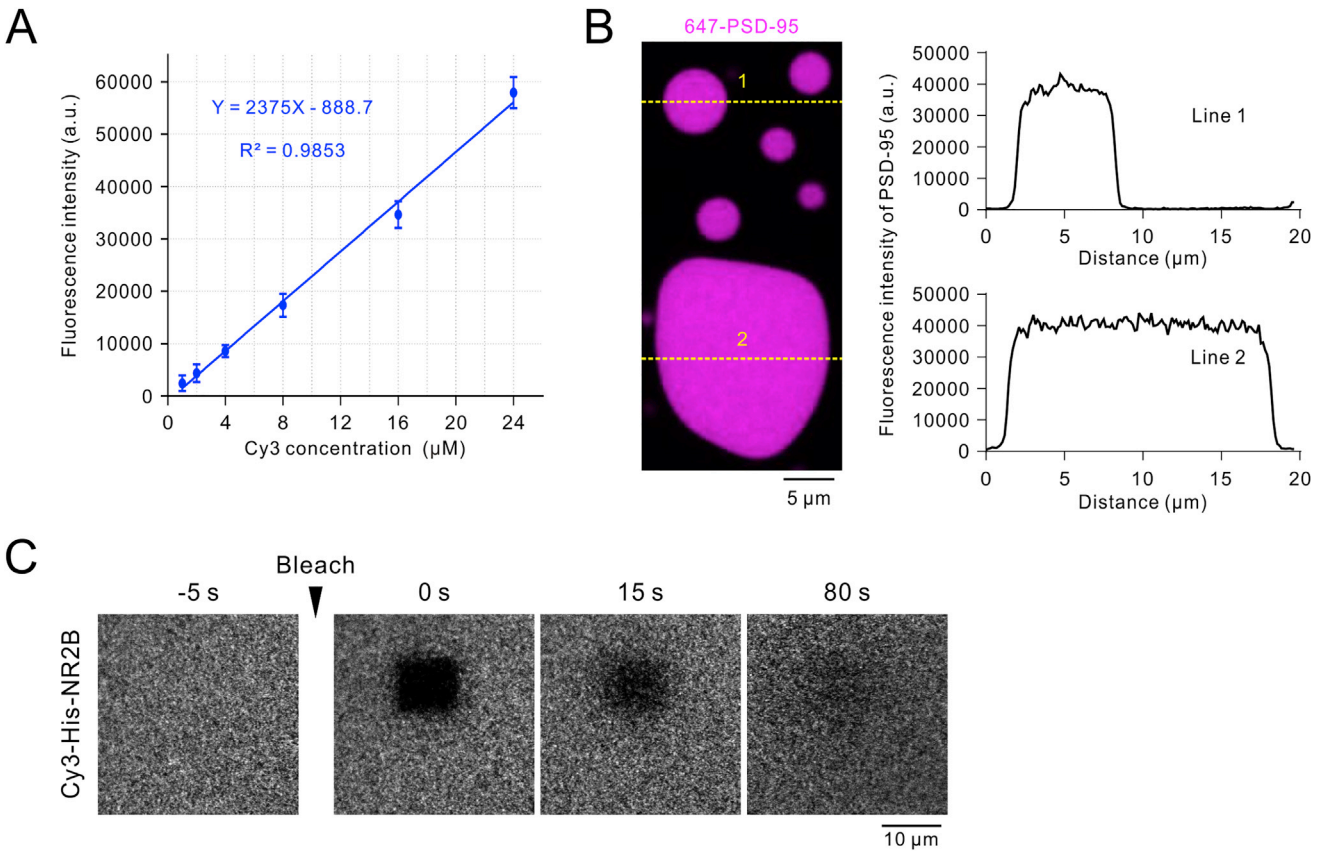

Figure S4. Confocal Microscope-Based Imaging Method to Quantify Concentrations of PSD Components in the Condensed Droplets and to Study His-NR2B Dynamics on Supported Lipid Bilayers, Related to Figures 3 and 5

(A) Standard curve showing the relationship between Cy3 concentration (measured by spectrophotometer) and Cy3 fluorescence intensity (measured by confocal microscope using the same parameters as in Figures 3A and 3B). The fluorescence intensity for each concentration of Cy3-labeled Shank3 was an average value of 9 repeated readings and data are presented as mean ± SD. Blue curve shows the linear regression analysis of the fluorescence intensities versus protein concentrations.

(B) Concentrations of PSD-95 in small and large droplets are same. Confocal images of Alexa 647-PSD-95 in condensates formed by the PSD-95 and SynGAP mixture (30 μM PSD-95 full length, 1% Alexa 647 labeling; 90 μM SynGAP CC-PBM; pH 7.8). Confocal optical section thickness was 0.9 μm. Fluorescence intensities along the dashed lines 1&2 from the same z-dimension layer are plotted at the right. The line plot indicates that PSD-95 in the two droplets with different sizes has the same concentration, and PSD-95 is uniformly distributed within each droplet.

(C) FRAP analysis showing that membrane anchored His-NR2B were evenly distributed and freely diffusible on the lipid bilayers before addition of the PSD scaffold proteins. His-NR2B was Cy3 labeled at 2% level. The Cy3 fluorescence signal in the bleached region recovered rapidly after photo-bleaching.

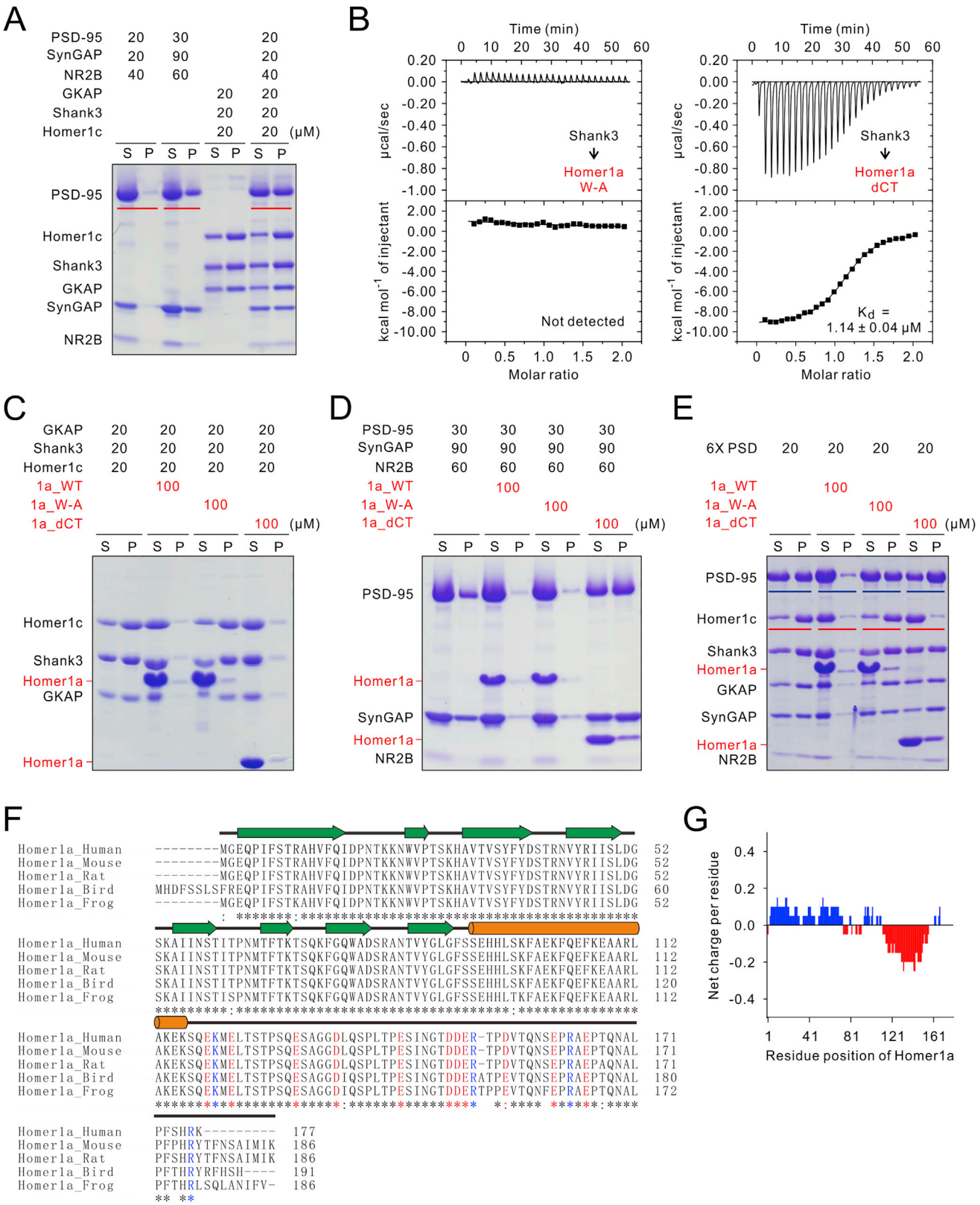

(legend on next page)

Figure S5. Mechanisms of Homer1a-Induced Dispersion of PSD Condensates, Related to Figures 4 and 6

(A) Sedimentation assay showing the Homer subgroup (GKAP/Shank3/Homer1c) promotes PSD-95 subgroup (PSD-95/SynGAP/NR2B) phase separation when the two subgroups were mixed at the concentration of 20 μM.

(B) ITC-based measurement comparing Shank3 (300 μM in the syringe) binding to Homer1a W-A and Homer1a dCT (30 μM in the cell). W24 to A mutation in Homer1a EVH1 domain totally abolished its Shank3 binding (*left*). Deleting the Homer1a-specific tail following the EVH1 domain had no impact on its binding to Shank3 (*right*, same as wild-type Homer1a in Figure 6A).

(C) Sedimentation assay showing excess amount of Homer1a (WT or dCT) but not Homer1a W-A disperses Homer subgroup phase separation through directly competing with Homer1c in binding to Shank3.

(D) Sedimentation assay showing excess amount of Homer1a (WT or W-A) disperses the PSD-95 subgroup phase separation. In contrast, Homer1a dCT enhances the PSD-95 subgroup phase separation.

(E) Sedimentation assay investigating different Homer1a proteins on the phase transition of the 6× PSD system. It is noticed that Homer1a dCT can weaken the Homer subgroup phase transition, but enhance the PSD-95 subgroup to form condensates.

(F) Sequence alignment of Homer1a from different species. β strand and α-helix structures on the EVH1 domain are labeled by green arrow and orange column, respectively. Negatively and positively charged residues on the C-terminal tail are highlighted by red and blue, respectively. It is noted that Homer1a contains a highly conserved, unstructured tail sequence with about 60 residues following its EVH1 domain (aa 117-end).

(G) Charge distribution pattern of Homer1a as a function of its residue number showing the prominent negatively charged tail (highlighted in red) of the protein.

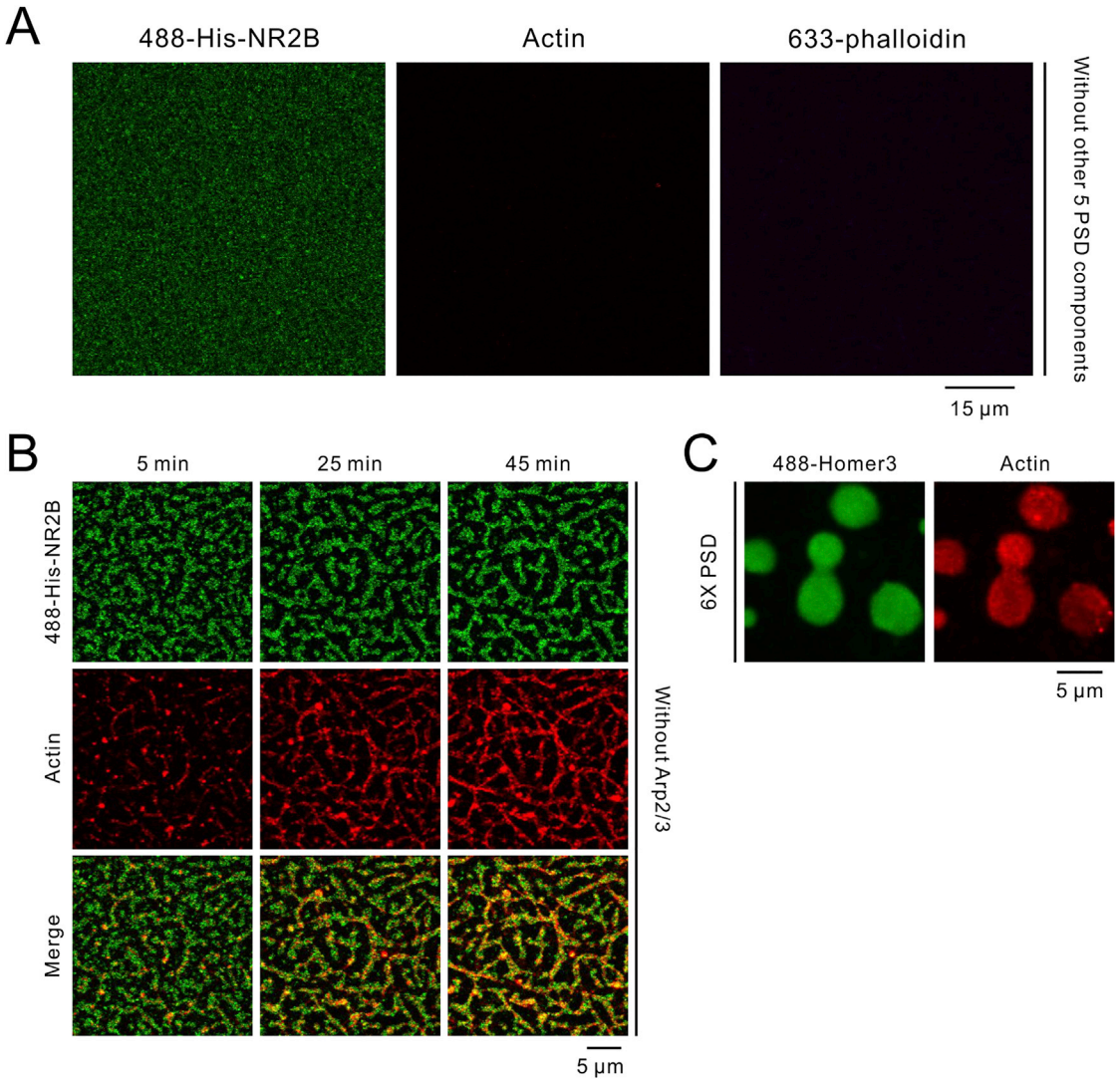

Figure S6. PSD Condensates-Mediated Promotion of Actin Bundle Formation, Related to Figure 7

(A) Without PSD condensates formation, Cortactin and Arp2/3 complex alone failed to promote actin polymerization on lipid bilayers. In this assay, 0.5 μM G-actin (5% Rhodamine-labeled), 0.2 μM Cortactin, 0.03 μM Arp2/3 complex and 0.03 μM Alexa 633-phalloidin were added to the NR2B-anchored lipid membrane bilayers (same concentrations as in Figure 7D). The rest of 5 PSD components were dropped out. Images were acquired ~100 min after addition of the actin polymerization complex.

(B) The 6× PSD condensates can promote actin bundle formation without Arp2/3. F-actin (Rhodamine labeled) polymerization on lipid bilayers overlaid with His-NR2B clusters (Alexa 488-labeled) in the absence of Arp2/3 (other conditions are identical to Figure 7D).

(C) Confocal imaging showing that 6× PSD droplets enrich G-actin. 0.5 μM G-actin (5% Rhodamine labeled) was added into 5 μM 6× PSD mixture with Alexa 488-Homer3 as the droplet marker.

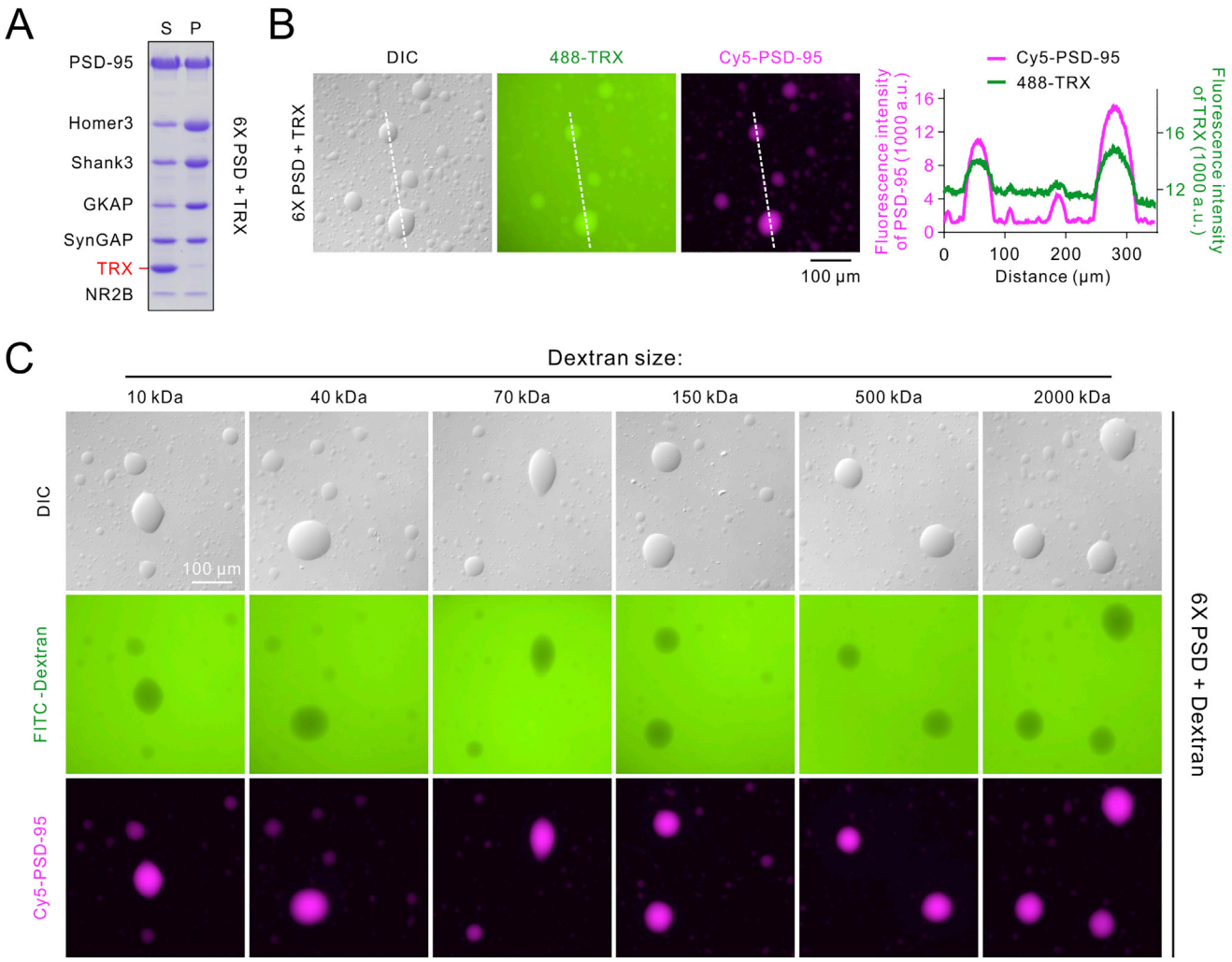

Figure S7. PSD-95 Determining the Gephyrin Exclusion from the Excitatory PSD Condensates, Related to Figure 7

(A) Sedimentation assay showing the S/P distribution of thioredoxin (40 μM) in the 6× PSD (20 μM) phase transition experiment.

(B) The PSD condensates are permeable to and slightly enriches 14 kDa thioredoxin. 20 μM Alexa 488-labeled TRX was added to the 6× PSD mixtures (20 μM, only PSD-95 was labeled by Cy5). Fluorescence intensities along the white dashed lines are analyzed at right.

(C) Dextrans with different sizes are all excluded by the 6× PSD droplets. 2 μM FITC-labeled dextrans with different sizes were added to 6× PSD mixtures (20 μM, only PSD-95 was labeled by Cy5). Images with 10 kDa and 2000 kDa dextrans were also presented in Figure 7H. Droplet morphologies were captured by DIC imaging. Dextran and PSD-95 fluorescence intensities along the white dashed lines above are analyzed below.